https://doi.org/10.5194/egusphere-2026-3864
Preprint. Discussion started: 17 July 2026

First comparison of XCO_2 products from DQ-1 ACDL and passive optical satellites

Yike Wang[1], Ge Han[1,3], Hongyuan Zhang[2], Yiyang Huang[1], Kangjie Zhou[1], Wei Gong[4,5]

[1] Hubei Key Laboratory of Quantitative Remote Sensing of Land and Atmosphere, School of Remote Sensing and Information Engineering, Wuhan University, Wuhan 430079, China
[2] State Key Laboratory of Information Engineering in Surveying, Mapping and Remote Sensing, Wuhan University, Luoyu Road No.129, Wuhan 430079, China
[3] Perception and Effectiveness Assessment for Carbon-neutrality Efforts, Engineering Research Center of Ministry of Education, Institute for Carbon Neutrality, Wuhan University, Wuhan, China
[4] Electronic Information School, Wuhan University, Wuhan, China
[5] Wuhan Institute of Quantum Technology, Wuhan, China

Correspondence to: Ge Han (udhan@whu.edu.cn)

Abstract. Spaceborne active CO_2 IPDA lidar provides an active remote-sensing approach for XCO_2 observations that differs from passive NIR/SWIR remote sensing. However, comparisons between DQ-1 ACDL and passive optical satellite XCO_2 products remain limited. Here we compare DQ-1 ACDL with OCO-2, OCO-3, GOSAT, and GOSAT-2 XCO_2 products from June 2022 to December 2024 using a unified framework that combines CAMS-based spatiotemporal coherence assessment, satellite sampling availability, daily 2° aggregation, spatiotemporal collocation, and XCO_2 column-definition correction. The results show that DQ-1 is broadly consistent with OCO-2 and OCO-3 over coherent and well-sampled regions, with mean differences mostly below 0.5 ppm and similar spatial distributions, meridional structures, and regional monthly variations. Nighttime DQ-1 XCO_2 is also consistent with CAMS-derived XCO_2, indicating stable performance relative to an external model reference. Independent validation against TCCON shows that daytime DQ-1 XCO_2 has a correlation coefficient of 0.92, a mean bias of 0.21 ppm, and an RMSE of 1.49 ppm, with statistics comparable to GOSAT. Regional results further indicate that DQ-1 does not simply duplicate existing passive satellite observations, but provides complementary XCO_2 observational coverage under high aerosol loading, at high latitudes, and in regions where passive observations are limited. Overall, DQ-1 ACDL is comparable to passive satellite XCO_2 products under the unified framework, and can serve as an important complement to existing passive satellite XCO_2 observations, supporting future active–passive joint XCO_2 constraints, regional carbon flux inversions, and emission monitoring.

https://doi.org/10.5194/egusphere-2026-3864
Preprint. Discussion started: 17 July 2026

1 Introduction

The continued accumulation of atmospheric carbon dioxide (CO_2) is one of the primary drivers of anthropogenic climate change and is a key variable for characterizing changes in the global carbon cycle, constraining surface sources and sinks, and assessing emission changes (Friedlingstein et al., 2026). Due to the high background concentration of atmospheric CO_2, perturbations caused by surface fluxes and atmospheric transport are typically only of ppm magnitude. Therefore, carbon-budget assessments, source–sink attribution, and emission estimates all rely on CO_2 observations with high precision and accuracy (Crowell et al., 2018; Kulawik et al., 2016). Ground-based observations provide high precision and temporal continuity and serve as an important foundation for carbon-cycle studies and satellite validation. However, their spatial coverage is limited and unevenly distributed. Satellite observations of the column-averaged dry-air mole fraction of CO_2 (XCO_2) can provide broader spatial coverage than ground-based observations and be assimilated into atmospheric inversion systems to constrain and quantify natural CO_2 fluxes and anthropogenic CO_2 emissions (Basu et al., 2018; Buchwitz et al., 2017; Keppel-Aleks et al., 2013; Wunch et al., 2011).

Over the past two decades, passive satellite observations based on solar-reflected near-infrared and shortwave-infrared (NIR/SWIR) spectra have developed into a relatively mature XCO_2 observing system and have become an important reference for evaluating new CO_2 remote-sensing techniques. The development of missions from SCIAMACHY to GOSAT, OCO-2/OCO-3, GOSAT-2, and TanSat has continuously improved global XCO_2 observing capability, retrieval algorithms, and the validation framework based on the Total Carbon Column Observing Network (TCCON) (Buchwitz et al., 2005; Kuze et al., 2016; Noël et al., 2021, 2022; O'Dell et al., 2018; Taylor et al., 2023; Yang et al., 2020). However, passive NIR/SWIR retrievals rely on radiance reflected by the surface or cloud tops under solar illumination, and their data availability and retrieval errors are influenced by solar zenith angle, surface reflectance, clouds and aerosols, and quality control. For example, although OCO-2 can acquire nearly one million soundings per day, typically only about 7 %–12 % of these soundings are retained after quality control and used for XCO_2 retrieval on monthly timescales (Crisp et al., 2017). Therefore, differences among passive XCO_2 products cannot be attributed simply to sensor biases. They usually reflect the combined effects of retrieval algorithms, quality control, sampling representativeness, and bias correction.

Active CO_2 remote sensing based on integrated path differential absorption (IPDA) lidar provides a physically distinct approach to XCO_2 observation compared with passive remote sensing based on reflected sunlight. This technique has been systematically investigated in earlier mission concepts and airborne demonstrations, including ASCENDS and A-SCOPE (Abshire et al., 2010, 2014; Amediek et al., 2017; Wang et al., 2014). For China's CO_2-IPDA satellite mission, previous studies have assessed instrument performance and the feasibility of urban CO_2 detection (Han et al., 2017, 2018). In April 2022, the Aerosol and Carbon Dioxide Lidar (ACDL) onboard the Atmospheric Environment Monitoring Satellite Da Qi-1 (DQ-1) was launched into orbit, bringing spaceborne active IPDA CO_2 sensing into on-orbit application. The CO_2 channel of ACDL operates near 1.57 μm and retrieves XCO_2 by measuring differential CO_2 absorption along the optical path with online and offline laser pulses (Mao et al., 2018; Zhang et al., 2024). Because its active light source does not depend on solar illumination,

https://doi.org/10.5194/egusphere-2026-3864
Preprint. Discussion started: 17 July 2026

ACDL has potential sampling advantages at night and at high latitudes, providing observations under conditions in which passive NIR/SWIR measurements are limited by solar illumination (Wang et al., 2014). Recent studies have reported the XCO_2 retrieval framework, global XCO_2 observation characteristics characteristics, and validation of DQ-1 ACDL against TCCON and passive satellite products, and have demonstrated its potential for diagnosing strong point sources, urban fossil-fuel CO_2 emissions, and power-plant emissions (Han et al., 2024, 2025; Shi et al., 2023; Yi et al., 2025, 2026; Zhang et al., 2024; Zhang et al., 2025). However, ACDL is not a simple alternative to passive NIR/SWIR sensors for XCO_2 measurements. They differ systematically in light-source dependence, footprint scale, day–night sampling, vertical sensitivity, and effective column definition. As a result, differences between their XCO_2 products may reflect contributions from real atmospheric variability, sampling representativeness, and observation-operator differences.

Beyond the independent validation of individual XCO_2 products, a more critical question is how active and passive XCO_2 products can be compared within a unified measurement-definition and sampling framework. Previous studies have examined the retrieval and validation of GOSAT/GOSAT-2 products (Noël et al., 2021, 2022), the consistency of OCO-2 and OCO-3 (Taylor et al., 2023), intercomparisons among multiple passive XCO_2 products (Fang et al., 2023; Kong et al., 2019; Liang et al., 2017; Yoshida et al., 2013), and the validation and emission applications of DQ-1 ACDL products (Han et al., 2024, 2025; Zhang et al., 2024; Zhang et al., 2025). These studies provide an important basis for understanding the error characteristics and application potential of different XCO_2 products. However, no systematic assessment has yet compared DQ-1 ACDL with GOSAT, GOSAT-2, OCO-2, and OCO-3 within a unified framework for spatiotemporal collocation, spatial aggregation, and correction of XCO_2 column-definition differences. If original satellite XCO_2 products from different satellites are compared directly, differences related to sampling representativeness and XCO_2 column definition cannot be separated, making the observed active–passive XCO_2 differences difficult to interpret. Therefore, before active and passive XCO_2 products are jointly used for flux inversion or emission monitoring, it is necessary to first quantify the comparability of these products within a unified comparison framework and characterize their bias and RMSE in relation to surface reflectance.

In this study, we use DQ-1 ACDL, OCO-2, OCO-3, GOSAT, and GOSAT-2 XCO_2 products from June 2022 to December 2024 to assess active–passive XCO_2 consistency and the remaining differences within a unified comparison framework. Through the selection of coherent and well-sampled comparison regions, daily gridded collocation, spatial aggregation, and column-definition correction, we quantify the differences between DQ-1 ACDL and passive satellite XCO_2 products. We further diagnose these differences using surface reflectance and independent validation results. The objective of this study is to evaluate the comparability of DQ-1 active IPDA XCO_2 observations with passive NIR/SWIR XCO_2 products and to provide a quantitative basis for future active–passive joint XCO_2 flux inversions and emission monitoring.

https://doi.org/10.5194/egusphere-2026-3864
Preprint. Discussion started: 17 July 2026

2 Data and methods

2.1 Datasets

The satellite XCO_2 products, CAMS CO_2 data, MODIS surface reflectance data, and TCCON ground-based observations used in this study are summarized in Table 1. This section introduces these datasets in relation to the active–passive XCO_2 consistency assessment, while the detailed processing and comparison methods are described in Sect. 2.2.

2.1.1 DQ-1 ACDL L2A XCO_2 product

The DQ-1/ACDL L2A XCO_2 product is used as the active lidar dataset in this study. The retrieval algorithm, error characterization, and quality-control procedure of the product are described in detail by Han et al. (2025). Ascending (Asc) and descending (Desc) observations are processed separately. Quality filtering retains only valid retrievals with QAflag = 1 or 5, where QAflag = 1 denotes a normal retrieval and QAflag = 5 denotes a normal retrieval with a high signal-to-noise ratio.

The main variables used in this study include XCO_2, XCO_2_uncertainty, Hour, Day_Flag, SurfacePressure, PressureLevel, and the vertical weighting function (WF). Here, XCO_2 represents the column-averaged CO_2 dry-air mole fraction for each valid ACDL observation, and XCO_2_uncertainty denotes the retrieval uncertainty reported in the product. Hour and Day_Flag are used to determine the observation time and day–night condition. SurfacePressure, PressureLevel, and WF characterize the effective ACDL integration column and vertical sensitivity, and are used in the correction for XCO_2 column-definition differences in Sect. 2.2.3. Because DQ-1 active lidar observations do not rely on solar illumination, daytime DQ-1 samples are used for the active–passive consistency assessment with passive satellite products, whereas nighttime DQ-1 samples are analyzed separately for the external model-reference diagnosis described in Sect. 2.2.6.

2.1.2 Passive satellite XCO_2 products

To evaluate the consistency between DQ-1 ACDL XCO_2 and passive NIR/SWIR satellite XCO_2 products, we use XCO_2 products from OCO-2, OCO-3, GOSAT, and GOSAT-2 as comparison datasets. These products mainly retrieve XCO_2 from solar-reflected near-infrared and shortwave-infrared absorption spectra; therefore, the observations generally correspond to daytime clear-sky or near-clear-sky conditions.

OCO-2 and OCO-3 are NASA Orbiting Carbon Observatory missions designed to retrieve XCO_2 from reflected solar spectra using three-channel high-resolution grating spectrometers and full-physics retrieval algorithms (Crisp et al., 2017; Eldering et al., 2017; O'Dell et al., 2018; Taylor et al., 2023). GOSAT and GOSAT-2 carry the Thermal And Near-infrared Sensor for carbon Observation Fourier Transform Spectrometer (TANSO-FTS) and its successor TANSO-FTS-2, respectively. Their instrument characteristics, retrieval algorithms, and XCO_2 products have been described in previous studies (Kuze et al., 2009, 2016; Noël et al., 2021, 2022; Suto et al., 2021; Yoshida et al., 2023). The passive satellite products are provided as individual soundings and provide the XCO_2 observations for comparison with DQ-1. The corresponding quality-control criteria

https://doi.org/10.5194/egusphere-2026-3864
Preprint. Discussion started: 17 July 2026

are summarized in Table 2, and the spatiotemporal collocation and column-definition correction are described in Sects. 2.2.2 and 2.2.3.

2.1.3 CAMS CO_2 profiles and column-averaged XCO_2 fields

We use the Copernicus Atmosphere Monitoring Service (CAMS) global greenhouse gas inversion CO_2 product as an external model reference field. The CAMS CO_2 inversion product used here is constrained by surface air-sample observations and generated by the PYVAR atmospheric inversion system, which is based on the LMDZ offline global atmospheric transport model. The product provides surface fluxes, model-level CO_2 dry-air mole fractions, and column-averaged XCO_2, among other variables (Chevallier et al., 2005, 2010).

CAMS is used in three main ways in this study. First, CAMS column-averaged XCO_2 is used to evaluate the spatial homogeneity and short-term temporal coherence within each 2° candidate grid cell, thereby identifying background regions that are more suitable for inter-satellite comparison. Second, CAMS model-level CO_2 profiles are used as a common external profile and are passed through the observation operators of different satellites to construct CAMS-derived XCO_2 values consistent with each satellite's column definition. This allows us to estimate the theoretical differences caused by differences in vertical sensitivity and effective column definition. Third, for nighttime DQ-1 observations, CAMS-derived XCO_2 is used as an external model reference to evaluate the consistency between nighttime DQ-1 XCO_2 and the model reference field. It should be emphasized that CAMS is not treated as the truth for satellite observations in this study, nor is it used to directly correct the absolute biases of the satellite products. The specific uses of CAMS are described in Sects. 2.2.1, 2.2.3, and 2.2.6.

2.1.4 MODIS Band 6 shortwave-infrared surface reflectance

To examine the potential influence of shortwave-infrared surface reflectance on the differences between DQ-1 and passive satellite XCO_2, we use the Aqua MODIS MYD09CMG.061 daily surface reflectance product. MYD09CMG is a Level-3 Climate Modeling Grid product that provides atmospherically corrected surface reflectance in the visible, near-infrared, and shortwave-infrared spectral regions (Vermote et al., 1997, 2002, 2008).

We select MYD09CMG Band 6 (1628–1652 nm) as a proxy for surface reflectance near the 1.6 μm CO_2 absorption region. This band is not the actual retrieval channel of any of the XCO_2 sensors and is not used for any XCO_2 correction. Instead, it is used only as a common indicator of surface optical conditions to diagnose whether the bias and RMSE between DQ-1 and passive satellite XCO_2 vary systematically with surface reflectance. The MODIS quality filtering, spatial aggregation, and reflectance binning methods are described in Sect. 2.2.4.

2.1.5 TCCON ground-based XCO_2 observations

We use the Total Carbon Column Observing Network (TCCON) GGG2020 data product as an independent ground-based validation reference. TCCON retrieves the column-averaged dry-air mole fraction of CO_2 from ground-based Fourier transform

https://doi.org/10.5194/egusphere-2026-3864
Preprint. Discussion started: 17 July 2026

spectrometer measurements of solar near-infrared absorption spectra, and it is widely used for the validation of OCO-2/OCO-3, GOSAT/GOSAT-2, and other satellite XCO_2 products (Noël et al., 2022; Taylor et al., 2023; Wunch et al., 2010, 2011).

Only TCCON XCO_2 observations that pass the official quality control are used in this study. Because TCCON relies on direct solar spectra, it is mainly used for the independent validation of daytime DQ-1 observations and passive satellite XCO_2 products, and it is not used for bias correction in the inter-satellite comparisons. The TCCON sites and valid observation periods used for validation are listed in Table A1. The satellite–TCCON spatiotemporal matching method is described in Sect. 2.2.5.

Table 1. Overview of the datasets used in this study.

Dataset	Product/version	Native resolution/scale	Period used
DQ-1 ACDL XCO_2	L2A XCO_2; Asc/Desc	Daily; individual soundings	Jun 2022–Dec 2024
OCO-2 XCO_2	OCO2_L2_Lite_FP.11.2r	Daily; individual soundings	Jun 2022–Dec 2024
OCO-3 XCO_2	OCO3_L2_Lite_FP.11r	Daily; individual soundings	Jun 2022–Dec 2024
GOSAT XCO_2	GOSAT SWIR L2 V03.05	Daily; individual soundings	Jun 2022–Dec 2024
GOSAT-2 XCO_2	GOSAT-2 SWIR L2 V02.20	Daily; individual soundings	Jun 2022–Dec 2024
CAMS CO_2 fields	CAMS73 v24r1 CO_2 inversion	3-hourly; 1° × 1°	Jun 2022–Dec 2024
MODIS surface reflectance	MYD09CMG.061	Daily; 0.05°	Jun 2022–Dec 2024
TCCON XCO_2	TCCON GGG2020	Site-level observations	Jun 2022–Dec 2024

2.2 Methods

To reduce the influence of real atmospheric gradients, observation-time differences, and uneven sensor sampling on inter-satellite XCO_2 comparisons, we first identify coherent and well-sampled comparison regions on a global 2° × 2° grid. Candidate grid cells are required to satisfy three conditions: weak spatial gradients in the CAMS background field within the grid cell, high consistency in short-term temporal variations among subgrid cells, and sufficient effective multi-sensor observational coverage. For this purpose, we construct a CAMS-based spatiotemporal coherence score and a satellite sampling availability score, and then determine the final comparison regions using a combined score. Based on these selected regions, all active–passive satellite comparisons are based on daily samples aggregated within selected 2° comparison grid cells, rather than direct footprint-level or point-by-point matching.

https://doi.org/10.5194/egusphere-2026-3864
Preprint. Discussion started: 17 July 2026

2.2.1 Selection of coherent and well-sampled comparison regions

(1) CAMS-based spatiotemporal coherence score

CAMS XCO_2 is first averaged to daily fields and then used to evaluate the internal consistency of each 2° × 2° grid cell. Because the native horizontal resolution of CAMS is 1° × 1°, each 2° grid cell contains up to four 1° subgrid cells. For day d and 2° grid cell g, the spatial dispersion of subgrid XCO_2 relative to the 2° grid-cell mean is defined as:

$$\sigma_{sp}(d,g) = \left[\frac{1}{N_g}\sum_{k=1}^{N_g}\left(X_{d,k} - \overline{X}_d(g)\right)^2\right]^{1/2} \tag{1}$$

Where $X_{d,k}$ denotes the daily mean XCO_2 for the 1° subgrid cell k on day d, $\overline{X}_d(g)$ is the daily mean XCO_2 of the corresponding 2° grid cell, and N_g is the number of valid subgrid cells. The quantity $\sigma_{sp}(d,g)$ represents the subgrid heterogeneity within a 2° grid cell on a given day. Over the study period, the median and 95th percentile of $\sigma_{sp}(d,g)$ are denoted as $\sigma_{sp,med}(g)$ and $\sigma_{sp,95}(g)$, respectively, and are used to characterize spatial heterogeneity under typical and highly dispersed conditions.

To evaluate whether short-term temporal variations are consistent among the 1° subgrid cells within the same 2° grid cell, a 30 d moving-mean background is removed from the daily XCO_2 time series of each subgrid cell to obtain a high-pass anomaly series:

$$X'_{d,k} = X_{d,k} - \tilde{X}^{30}_{d,k} \tag{2}$$

Where $X'_{d,k}$ denotes the high-pass XCO_2 anomaly for kth subgrid cell on day d, and $\tilde{X}^{30}_{d,k}$ denotes the 30 d moving-mean background. Let P be the set of pairwise combinations of 1° subgrid cells within the 2° grid cell g. The temporal consistency index is then defined as:

$$TCI(g) = \frac{1}{N_P}\sum_{(p,q)\in P} corr_d\left(X'_{d,p}, X'_{d,q}\right) \tag{3}$$

where $corr_d$ denotes the Pearson correlation coefficient calculated from the daily anomaly series. A higher $TCI(g)$ indicates more consistent short-term XCO_2 temporal variations within the grid cell.

To describe whether the relative differences among subgrid cells remain stable over time, the stability of internal spatial differences is defined as:

$$SDI(g) = \frac{1}{N_P}\sum_{(p,q)\in P} std_d\left(X_{d,p} - X_{d,q}\right) \tag{4}$$

where std_d denotes the standard deviation calculated along the time dimension. Grid cells with fewer than 60 valid days are excluded from the scoring procedure to avoid unstable correlation and percentile statistics caused by overly short time series.

The quantities $\sigma_{sp,med}$, $\sigma_{sp,95}$, TCI, and SDI are then normalized using the 5th and 95th percentiles across all valid 2° grid cells and clipped to the range 0–1. Lower values of $\sigma_{sp,med}$, $\sigma_{sp,95}$, and SDI indicate higher coherence; therefore, their normalized values are reversed. In contrast, higher TCI values indicate stronger temporal consistency. The final CAMS-based spatiotemporal coherence score is defined as:

$$S_{CAMS}(g) = \frac{H_{sp,med}(g)+H_{sp,95}(g)+C_{TCI}(g)+H_{SDI}(g)}{4} \tag{5}$$

where $H_{sp,med}(g)$, $H_{sp,95}(g)$, $C_{TCI}(g)$, and $H_{SDI}(g)$ are the four normalized components. A higher $S_{CAMS}(g)$ indicates that the CAMS XCO_2 field within the 2° grid cell has lower spatial dispersion, more stable internal spatial differences, and more coherent short-term temporal variability.

(2) Multi-satellite sampling availability score

To ensure stable multi-satellite observational coverage in the candidate 2° grid cells, we construct a satellite sampling availability score. For each satellite, daily XCO_2 observations after quality control are first assigned to the same 2° grid according to the latitude and longitude of the observation center. Following the grid-based spatial-coverage method of Han et al. (2024) and the path-length-based definition of valid gridded observations described by Han et al. (2025), we do not use the raw number of observations as the only criterion for determining valid gridded observations. Instead, for each sensor, day, and grid cell, we calculate the along-track sampling length by accumulating the great-circle distances between adjacent valid observation centers along the same orbit track. For each sensor and day, only grid cells with an accumulated sampling length greater than or equal to half of the diagonal length of the local 2° grid cell are counted as valid observation days. The number of valid observation days is then accumulated over the study period and normalized to the range 0–1 using the 95th percentile among grid cells with positive values, yielding the satellite sampling availability score.

On this basis, the mean sampling availability of the main sensors is calculated by averaging $A_s(g)$:

$$A_{mean}(g) = \frac{1}{n_s}\sum_{s=1}^{n_s} A_s(g) \tag{6}$$

where $A_{mean}(g)$ represents the overall sampling sufficiency of grid cell $A_{mean}(g)$, $A_s(g)$ is the normalized valid-observation-day score for sensor s, and n_s is the number of sensors included in the main score (n_s = 5). These sensors include daytime DQ-1, OCO-2, OCO-3, GOSAT, and GOSAT-2.

To avoid high scores being dominated by a single sensor, we further calculate the sampling evenness among sensors:

$$E_{sensor}(g) = -\frac{\sum_{s=1}^{n_s} p_s(g)\ln p_s(g)}{\ln n_s} \tag{7}$$

$$p_s(g) = \frac{H_s(g)}{\sum_{s=1}^{n_s} H_s(g)} \tag{8}$$

where $E_{sensor}(g)$ is the Shannon evenness calculated from the sensor contribution fractions. It is higher when the contributions from multiple sensors are more balanced and lower when the valid observation days are dominated by a single sensor. Here, $p_s(g)$ denotes the fraction of valid observation days contributed by sensor s in grid cell g, calculated as the accumulated valid observation days $H_s(g)$ of sensor s divided by the total accumulated valid observation days from all sensors.

The multi-sensor same-day sampling support is defined as:

$$C_{multi}(g) = \min\left[\frac{D_{multi}(g)}{P_{95}(D_{multi}>0)}, 1\right] \tag{9}$$

https://doi.org/10.5194/egusphere-2026-3864
Preprint. Discussion started: 17 July 2026

where $C_{multi}(g)$ represents the same-day multi-sensor observation support for grid cell g. It is obtained by normalizing $D_{multi}(g)$, the accumulated number of days on which at least two main sensors satisfy the valid-observation condition on the same day, using its 95th percentile.

The final satellite sampling availability score is defined as:

$$S_{SAT}(g) = \frac{A_{mean}(g)+E_{sensor}(g)+C_{multi}(g)}{3} \quad (10)$$

where $S_{SAT}(g)$ accounts for mean sampling sufficiency, sampling evenness among sensors, and same-day multi-sensor observation support.

(3) Final score and selection of comparison regions

The final comparison-region score is determined jointly by the CAMS-based spatiotemporal coherence score and the satellite sampling availability score. To ensure both background-field coherence and sufficient multi-satellite sampling, we define the final score as the geometric mean of the two component scores:

$$S_{final}(g) = \sqrt{S_{CAMS}(g)S_{SAT}(g)} \quad (11)$$

where $S_{final}(g)$ denotes the final score for grid cell g. For the final selection, the 90th percentile of S_{final} is calculated separately for land and ocean grid cells. The 2° grid cells with S_{final} greater than or equal to the corresponding land or ocean threshold are retained as the final comparison regions.

2.2.2 Inter-satellite spatiotemporal collocation and sample selection

The quality-control criteria applied to each satellite XCO_2 product are listed in Table 2. Inter-satellite comparisons are based on daily samples aggregated within selected 2° comparison grid cells, rather than on matching individual soundings or footprints. After quality control, valid XCO_2 observations are assigned to the selected 2° comparison grid cells according to the latitude and longitude of their observation centers. For each date and selected grid cell, the daily mean XCO_2 and the mean observation time are then calculated. Inter-satellite collocation is based on daily gridded samples. A sample pair is considered a candidate pair only when the two products fall within the same selected 2° comparison grid cell on the same date and both satisfy the valid-observation-day criterion defined in Sect. 2.2.1. Candidate pairs are retained as final paired samples only if the difference between their daily mean observation times does not exceed 4 h. All subsequent inter-satellite differences are calculated as the XCO_2 of the product under evaluation minus that of the reference product.

Table 2. Quality-control criteria for the satellite XCO_2 products.

Satellite product	Quality-control and surface-type screening	Valid XCO_2 range
DQ-1 ACDL XCO_2	QAflag = 1 or 5; Asc/Desc processed separately	380~480 ppm
OCO-2 XCO_2	xco2_quality_flag = 0; land and ocean-glint observations retained	380~480 ppm

OCO-3 XCO_2	xco2_quality_flag = 0; land and ocean-glint observations retained	380~480 ppm
GOSAT XCO_2	totalPreScreeningResult = 0; totalPostScreeningResult = 0; Land: landFraction ≥ 80%; ocean-glint: landFraction ≤ 20% and sunglint flag = 1	380~480 ppm
GOSAT-2 XCO_2	xco2_quality_flag = 0; Land: landFraction ≥ 80%; ocean-glint: landFraction ≤ 20% and sunglintFlag = 1	380~480 ppm

2.2.3 Correction for XCO_2 column-definition differences among satellites

Different satellite XCO_2 products do not necessarily share the same effective column definition because they differ in prior profiles, pressure weighting functions, column averaging kernels, and vertical sensitivities. If the retrieved XCO_2 values are compared directly, part of the difference may arise from differences in the observation operators, rather than from real atmospheric CO_2 differences. To reduce this effect, we use CAMS 3-hourly CO_2 profiles as a common external reference profile and apply the observation operator of each satellite to these profiles to estimate the theoretical difference caused by XCO_2 column-definition differences.

For a given satellite s, the CAMS-derived XCO_2 under the column definition of that satellite is expressed as:

$$X_s^{\mathrm{CAMS}} = \mathcal{H}_s(c^{\mathrm{CAMS}}) \tag{12}$$

where $\mathcal{H}_s$ is the XCO_2 observation operator of satellite s, and c^{CAMS} is the CAMS CO_2 profile.

For the passive products from OCO-2, OCO-3, GOSAT, and GOSAT-2, c^{CAMS} is interpolated to the pressure levels of the corresponding product and then used together with the product-specific pressure weights and column averaging kernels to calculate XCO_2:

$$X_s^{\mathrm{CAMS}} = X_s^a + \sum_{k=1}^{n_s} w_{s,k} A_{s,k} \left[c_k^{\mathrm{CAMS}} - c_{s,k}^a\right] \tag{13}$$

where X_s^a is the prior XCO_2 of satellite s, $w_{s,k}$ and $A_{s,k}$ are the pressure weight and column averaging kernel for layer k, respectively, $c_{s,k}^a$ is the prior CO_2 mixing ratio, and c_k^{CAMS} is the CAMS CO_2 mixing ratio interpolated to the corresponding pressure level $p_{s,k}$.

For DQ-1/ACDL, the active lidar retrieval uses the weighting function (WF) to describe vertical sensitivity. The CAMS profile is therefore integrated using the DQ-1 WF and the effective pressure thickness:

$$X_{\mathrm{DQ1}}^{\mathrm{CAMS}} = \frac{\sum_{k=1}^{m} c^{\mathrm{CAMS}}(p_k) WF_k \Delta p_k}{\sum_{k=1}^{m} WF_k \Delta p_k} \tag{14}$$

where WF_k is the DQ-1 weighting function for layer k, and Δp_k is the effective pressure thickness of that layer.

For each satellite sample pair satisfying the spatiotemporal collocation criteria, s denote the product under evaluation and r denote the reference product. The theoretical XCO_2 column-definition difference caused by differences in the observation operators is then defined as:

$$\Delta X_{r-s}^{\mathrm{def}} = X_r^{\mathrm{CAMS}} - X_s^{\mathrm{CAMS}} \tag{15}$$

https://doi.org/10.5194/egusphere-2026-3864
Preprint. Discussion started: 17 July 2026

This definition difference is subsequently added to the observed XCO_2 of the product under evaluation, thereby converting it to the XCO_2 definition of the reference product:

$$X_{s\to r}^{\mathrm{corr}} = X_s^{\mathrm{obs}} + \Delta X_{r-s}^{\mathrm{def}} \tag{16}$$

This correction only accounts for the theoretical difference produced when the same CO_2 profile is represented under different satellite column definitions. CAMS is used only to estimate column-definition differences and is not treated as a truth reference for correcting satellite biases. The term $\Delta X_{r-s}^{\mathrm{def}}$ reflects only differences in the observation operators and effective column definitions. The differences after this correction may still include contributions from instrumental errors, retrieval errors, spatiotemporal sampling differences, and uncertainties in the CAMS CO_2 profiles.

2.2.4 Diagnosis of DQ-1–OCO-2/OCO-3 XCO_2 residuals using MODIS surface reflectance

The MODIS MYD09CMG Band 6 shortwave-infrared surface reflectance is used only to diagnose the influence of surface optical conditions on the DQ-1–OCO-2/OCO-3 XCO_2 differences. It is not used for any XCO_2 correction. For the DQ-1–OCO-2 and DQ-1–OCO-3 paired samples that have passed the spatiotemporal collocation and XCO_2 column-definition correction procedures, we extract the mean MODIS Band 6 reflectance within the same selected 2° comparison grid cell on the same day. Only samples with reflectance values between 0 and 1 and with at least 10 valid MODIS subpixels are retained, to reduce the influence of anomalous reflectance values on the statistics.

For each selected 2° grid cell, we then calculate the mean reflectance, mean bias, and RMSE. The RMSE is defined as the square root of the mean squared residuals of all valid paired samples within the same grid cell. Based on these 2° grid-cell statistics, the samples are further binned according to the grid-cell mean reflectance. A reflectance bin width of 0.05 is used for all samples and land samples, whereas a bin width of 0.02 is used for ocean samples to account for the smaller range of shortwave-infrared reflectance over the ocean. Statistics are calculated for a reflectance bin only when it contains at least 10 valid 2° grid cells. Within each reflectance bin, bias and RMSE are reported as the arithmetic means of the grid-cell mean bias values and grid-cell RMSE values, respectively. The error bars indicate the standard deviations of the corresponding 2° grid-cell statistics within the same reflectance bin.

2.2.5 Independent validation with TCCON observations

TCCON is used only as an independent ground-based validation reference and is not used to correct the inter-satellite biases. Following the validation approach for DQ-1/ACDL described by Han et al. (2025), we construct a 1° × 1° spatial matching window centered on each TCCON site and extract quality-controlled TCCON XCO_2 observations within ±0.5 h of the satellite overpass time. If multiple TCCON observations are available within the matching window, their median value is used as the reference. For the matched satellite samples, we estimate and correct the definition difference caused by differences in XCO_2 column definition and vertical sensitivity following Sect. 2.2.3. The corrected satellite XCO_2 is then compared with the TCCON reference value, and bias, RMSE, and the Pearson correlation coefficient are calculated.

https://doi.org/10.5194/egusphere-2026-3864
Preprint. Discussion started: 17 July 2026

2.2.6 Comparison of nighttime DQ-1 XCO_2 with CAMS-derived XCO_2

Because passive shortwave-infrared satellites and TCCON do not provide nighttime XCO_2 observations, CAMS CO_2 is used as an external model reference field for evaluating nighttime DQ-1 CO_2. We first select nighttime DQ-1 L2A observations that pass quality control, are located within the selected comparison regions, and satisfy the valid-observation-day condition defined in Sect. 2.2.1. These observations are then aggregated by date and selected 2° comparison grid cell. XCO_2, WF, SurfacePressure, and Hour are averaged arithmetically over the valid observations within each grid cell.

The nearest CAMS CO_2 profile is then matched according to the mean DQ-1 observation time. Using the aggregated WF and SurfacePressure, the CAMS profile is converted to XCO_2 under the DQ-1 column definition. The resulting CAMS-derived XCO_2 is finally paired with nighttime DQ-1 XCO_2, and bias, RMSE, and the Pearson correlation coefficient are calculated. The difference is defined as DQ-1 minus CAMS-derived XCO_2. This comparison is used to evaluate the consistency and stability of nighttime DQ-1 relative to an external model reference field, and should not be interpreted as an independent absolute validation against observations.

3 Results

3.1 Multi-satellite XCO_2 sampling coverage and temporal stability

Figure 1 shows the cumulative number of valid observing days for each satellite product on the unified 2° grid, revealing substantial differences in spatial sampling capability among the sensors. DQ-1 Asc and Desc both show relatively continuous global coverage, with stable sampling coverage between 60° S and 60° N. The two orbital directions exhibit similar spatial patterns but different local sampling intensities, indicating that the ascending and descending orbits provide complementary sampling. OCO-2 has relatively high overall coverage, but still shows pronounced orbital stripes because of the combined effects of its sun-synchronous orbit, observation modes, and cloud screening. OCO-3, installed on the International Space Station (ISS), has denser sampling at low and mid-latitudes but limited high-latitude coverage because of the non-sun-synchronous ISS orbit, limited orbital inclination, and platform viewing geometry (Taylor et al., 2023). In contrast, GOSAT and GOSAT-2 follow sparse point-sampling patterns, and their gridded coverage and cumulative valid-observation days are generally lower than those of DQ-1 and the OCO series.

The zonal totals further show that DQ-1 provides more spatially uniform sampling across most latitude bands. After combining Asc and Desc observations, the number of valid observations is markedly higher than that of either individual orbit and exceeds that of any single passive satellite product in most latitude bands. OCO-2 and OCO-3 also reach relatively high sample counts in some latitude bands, but their zonal variability is stronger, reflecting the greater sensitivity of passive observations to orbital sampling, observation mode, and cloud screening (Taylor et al., 2023). This feature is also consistent with previous comparisons of DQ-1, OCO-2, and OCO-3 coverage, which showed that OCO-3 has limited high-latitude coverage because of its orbital inclination and that the number of valid passive optical observations can be substantially reduced in regions affected by high aerosol loading or clouds (Han et al., 2024). The zonal valid-observation counts of GOSAT and

https://doi.org/10.5194/egusphere-2026-3864
Preprint. Discussion started: 17 July 2026

GOSAT-2 are generally low. GOSAT-2 shows some improvement relative to GOSAT, but still mainly provides long-term sparse sampling.

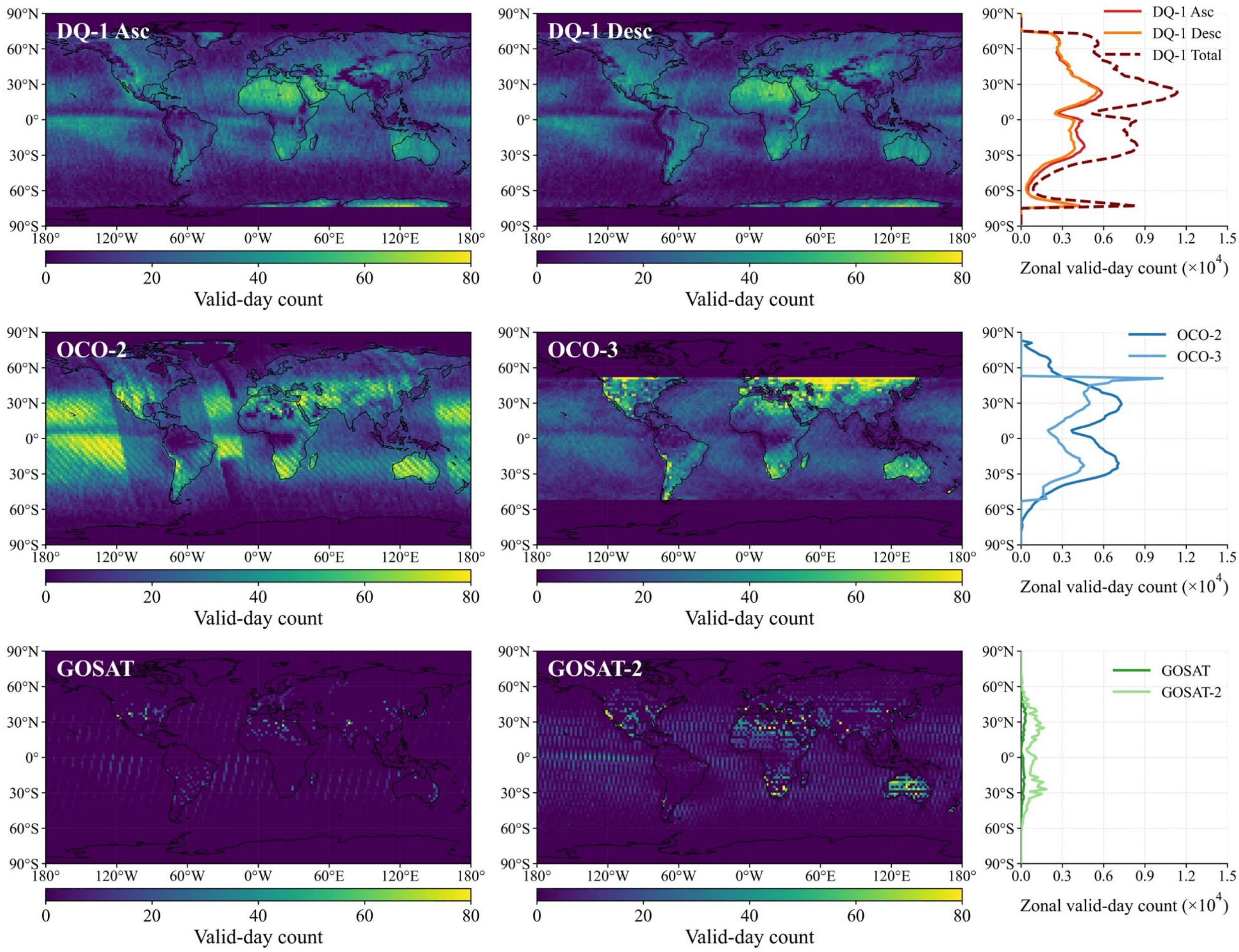

Figure 1. Spatial distributions and zonal totals of cumulative valid-observation days for the satellite XCO_2 products at 2° × 2° resolution.

The monthly statistics are shown in Fig. 2. The mean monthly numbers of valid observation cell-days for DQ-1 Asc and Desc are 0.77×10^4 and 0.71×10^4 cell-days, respectively, and the combined Asc+Desc value is approximately 1.48×10^4 cell-days. This value is higher than that of OCO-2, which is 0.99×10^4 cell-days, indicating that the combined DQ-1 Asc/Desc observations provide greater cumulative sampling. OCO-3 has a mean value of approximately 0.61×10^4 cell-days, but exhibits large month-to-month variability. In particular, the number of valid observations decreases markedly from November 2023 to June 2024, mainly associated with the temporary stowage and payload reconfiguration of OCO-3 on the ISS platform rather than with the quality filtering applied in this study. GOSAT-2 and GOSAT have much lower mean monthly values, approximately 0.14×10^4 and 0.03×10^4 cell-days, respectively. Overall, a single satellite is unlikely to provide both globally

https://doi.org/10.5194/egusphere-2026-3864
Preprint. Discussion started: 17 July 2026

continuous coverage and temporally stable sampling, whereas multi-source satellite observations can offer complementary advantages in spatial coverage and temporal stability.

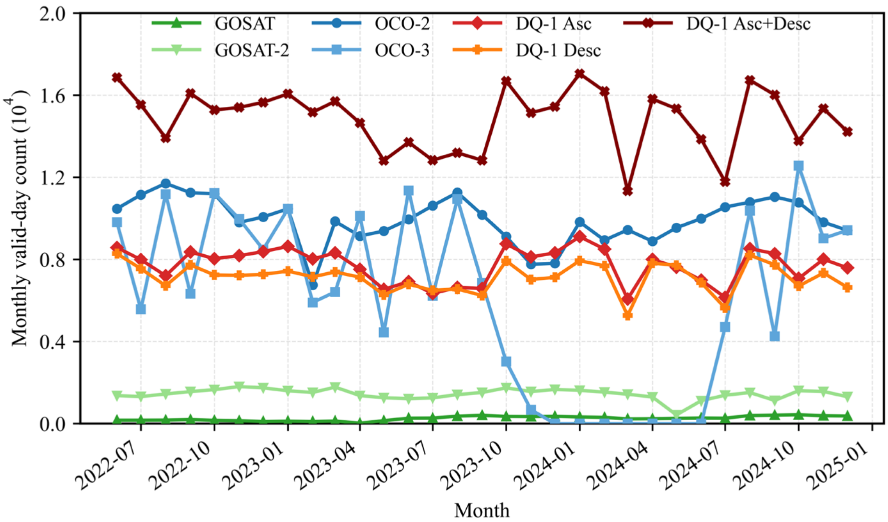

Figure 2. Monthly variations in valid-observation cell-days for the satellite XCO_2 products.

3.2 Coherent and well-sampled comparison regions

Figure 3 shows the CAMS-based spatiotemporal coherence score (CAMS score), the satellite sampling availability score (SAT score), the Final score, and the selected 2° comparison grid cells. The CAMS score is generally higher over open-ocean regions and areas with weak XCO_2 background gradients, including parts of the low- and middle-latitude oceans and the open Southern Hemisphere oceans. In contrast, lower CAMS scores occur over land–ocean transition zones, strong source–sink regions, complex-terrain areas, and land regions with strong XCO_2 spatial gradients, indicating larger subregional XCO_2 variability in these areas. The spatial distribution of the SAT score is mainly controlled by multi-sensor sampling availability. High SAT scores are concentrated in regions with relatively frequent repeated observations from multiple satellites, including North Africa–Arabia, Europe–Central Asia, East Asia, Australia, and several oceanic sampling bands. In contrast, lower SAT scores occur at high latitudes, in regions strongly affected by cloud and aerosol filtering, and over sparsely sampled ocean areas.

The final score jointly reflects background-field coherence and multi-satellite sampling availability. Based on this score, we selected 1297 2° comparison grid cells, including 540 land grid cells and 757 ocean grid cells. The selected land regions are mainly distributed over North Africa–Arabia, Central Asia, Europe, Australia, and parts of North America, whereas the selected ocean regions are mainly located over open oceans at low and middle latitudes. These selected regions define the spatial domain for the subsequent daily paired comparisons between active DQ-1 and passive XCO_2 products, and provide a set of regional samples with relatively stable background conditions and sufficient sampling support for the inter-satellite consistency assessment.

https://doi.org/10.5194/egusphere-2026-3864
Preprint. Discussion started: 17 July 2026

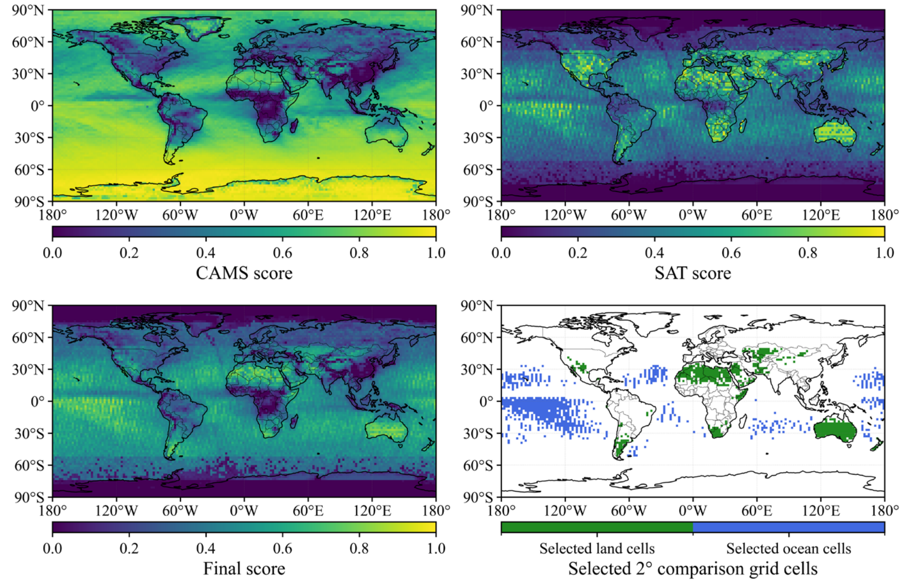

Figure 3. Spatial distributions of the CAMS-based coherence score, satellite sampling availability score, final score, and selected 2° comparison grid cells.

3.3 Inter-satellite XCO_2 consistency over the selected comparison regions

Figure 4 and Table A2 summarize the pairwise consistency statistics for the five satellite XCO_2 products over the selected comparison regions. The passive satellite products generally show high consistency with one another, with correlation coefficients R mostly around 0.9 for both land and ocean samples. The agreement between OCO-2 and OCO-3 is the strongest, with R = 0.97 over land and R = 0.99 over ocean, mean biases of −0.30 and −0.08 ppm, and RMSE values of 0.81 and 0.45 ppm, respectively. GOSAT is also broadly consistent with OCO-2 and OCO-3 over land, with R = 0.91–0.94 and RMSE values of 1.03–1.38 ppm. Over ocean, however, GOSAT is approximately 1.3 ppm higher than OCO-2 and OCO-3, indicating that differences among passive satellite XCO_2 products remain over ocean scenes.

In contrast, GOSAT-2 shows more pronounced differences from the other passive satellites. Relative to OCO-2 and OCO-3, GOSAT-2 exhibits positive biases of approximately 2.9–3.8 ppm over both land and ocean. Relative to GOSAT, the mean biases values of GOSAT-2 are 4.68 ppm over land and 2.79 ppm over ocean. Pairs involving GOSAT-2 also generally have higher RMSE values, mostly around 3–5 ppm, suggesting that GOSAT-2 is systematically higher than the other passive satellite products within the unified comparison framework used in this study. This systematic positive bias may be related to the fact that the GOSAT-2 SWIR L2 product used here has not been empirically bias corrected (Yoshida et al., 2023).

For the comparisons between DQ-1 and the passive satellite products, DQ-1 is generally consistent with OCO-2, OCO-3, and GOSAT. The DQ-1 comparisons with the OCO series show the closest agreement. For land and ocean samples, the DQ-1–OCO-2/OCO-3 comparisons yield R = 0.86–0.93, mean biases of 0.06–0.49 ppm, and RMSE values of 1.26–1.74 ppm.

https://doi.org/10.5194/egusphere-2026-3864
Preprint. Discussion started: 17 July 2026

In particular, the mean biases of DQ-1 relative to OCO-2 and OCO-3 are both smaller than 0.5 ppm, indicating that active IPDA XCO_2 from DQ-1 is broadly consistent with the passive OCO products over the selected comparison regions. Compared with GOSAT, DQ-1 also shows high consistency over land, with R = 0.90, mean bias = 0.76 ppm, and RMSE = 1.47 ppm. Over ocean, however, DQ-1 is lower than GOSAT by approximately 1.39 ppm, and the RMSE increases to 2.30 ppm, consistent with the result that GOSAT is higher than the OCO products over ocean.

Overall, the RMSE values for the DQ-1 comparisons with passive products are higher over ocean than over land, suggesting larger scatter in active–passive XCO_2 pairings under ocean-glint conditions. Because DQ-1 shows the highest consistency with OCO-2 and OCO-3 and these comparisons have the largest matched sample sizes, the subsequent analysis focuses on the spatial distributions of DQ-1–OCO-2/OCO-3 residuals and their relationship with MODIS Band 6 surface reflectance.

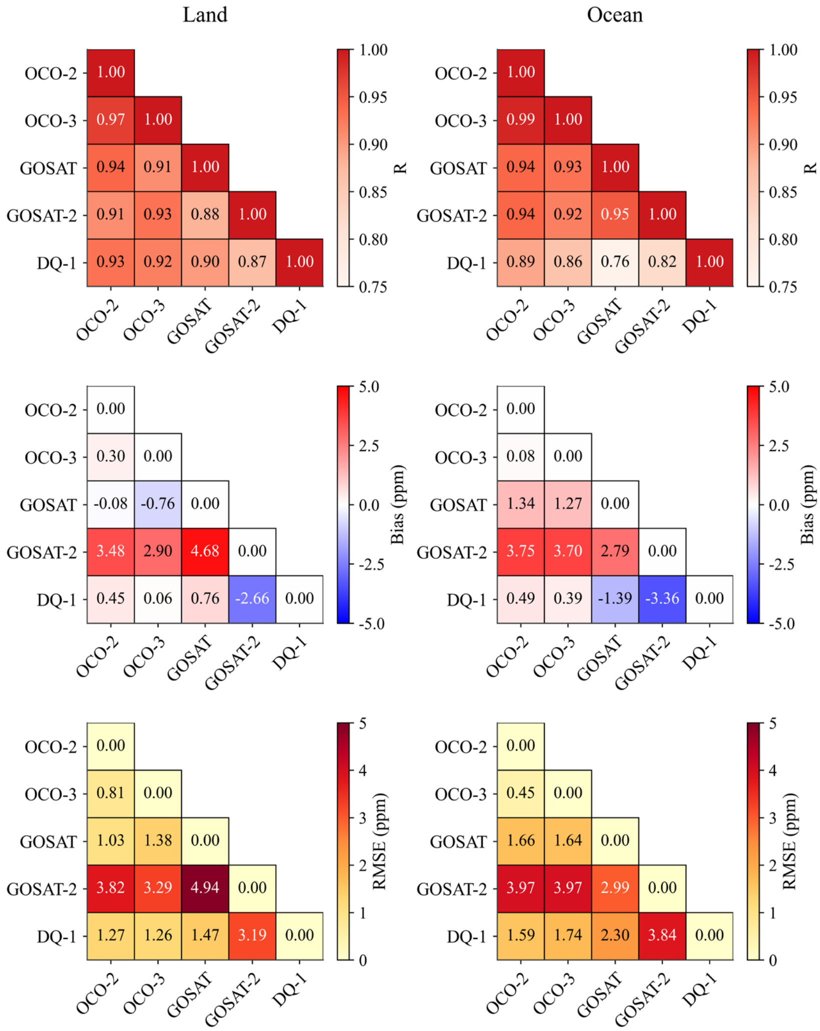

Figure 4. Pairwise consistency metrics for the satellite XCO_2 products over land and ocean in the selected comparison regions.

https://doi.org/10.5194/egusphere-2026-3864
Preprint. Discussion started: 17 July 2026

3.4 Spatial, zonal, and reflectance-based diagnosis of DQ-1–OCO-2/OCO-3 XCO_2 differences

3.4.1 Spatial and zonal differences in XCO_2 between DQ-1 and OCO-2/OCO-3

Figure A1 compares the spatial distributions of DQ-1, OCO-2, and OCO-3 XCO_2 over the selected 2° comparison grid cells. Overall, the three products show similar large-scale XCO_2 gradients, with higher values mainly over Northern Hemisphere land and lower values over Southern Hemisphere oceans. The high- and low-XCO_2 patterns in DQ-1 are broadly consistent with those of OCO-2 and OCO-3, indicating that active IPDA and passive NIR/SWIR XCO_2 products have similar spatial structures over the selected comparison regions.

Figure 5 further shows the spatial distributions of the mean DQ-1–OCO-2 and DQ-1–OCO-3 differences, together with the corresponding zonal-mean results. Spatially, most DQ-1–OCO-2 and DQ-1–OCO-3 differences are within approximately ±1 ppm, with no clear global-scale systematic bias. Local positive differences occur mainly over several oceanic sampling bands, Australia, and some low- and middle-latitude land regions, whereas negative differences are scattered over North Africa, Eurasia, and parts of the tropical oceans. This pattern suggests that the residual differences are more regional and sampling-dependent than globally systematic.

The zonal-mean results show that DQ-1 and OCO-2/OCO-3 have broadly consistent meridional XCO_2 variations, with higher values in the Northern Hemisphere mid-latitudes and lower values in the Southern Hemisphere. The zonal-mean values of DQ-1 and OCO-2 are approximately 420.15 and 419.74 ppm, respectively, corresponding to a mean difference of about 0.41 ppm. For the DQ-1–OCO-3 comparison, the corresponding values are approximately 419.17 and 419.00 ppm, with a mean difference of about 0.17 ppm. In most latitude bands, the DQ-1–OCO-2/OCO-3 differences are close to zero, with only small positive or negative deviations in some low- and middle-latitude regions. Overall, DQ-1 is consistent with OCO-2 and OCO-3 in both spatial distribution and meridional structure, indicating that the residual differences between active and passive XCO_2 products are generally small after applying unified filtering, aggregation, collocation, and column-definition correction.

https://doi.org/10.5194/egusphere-2026-3864
Preprint. Discussion started: 17 July 2026

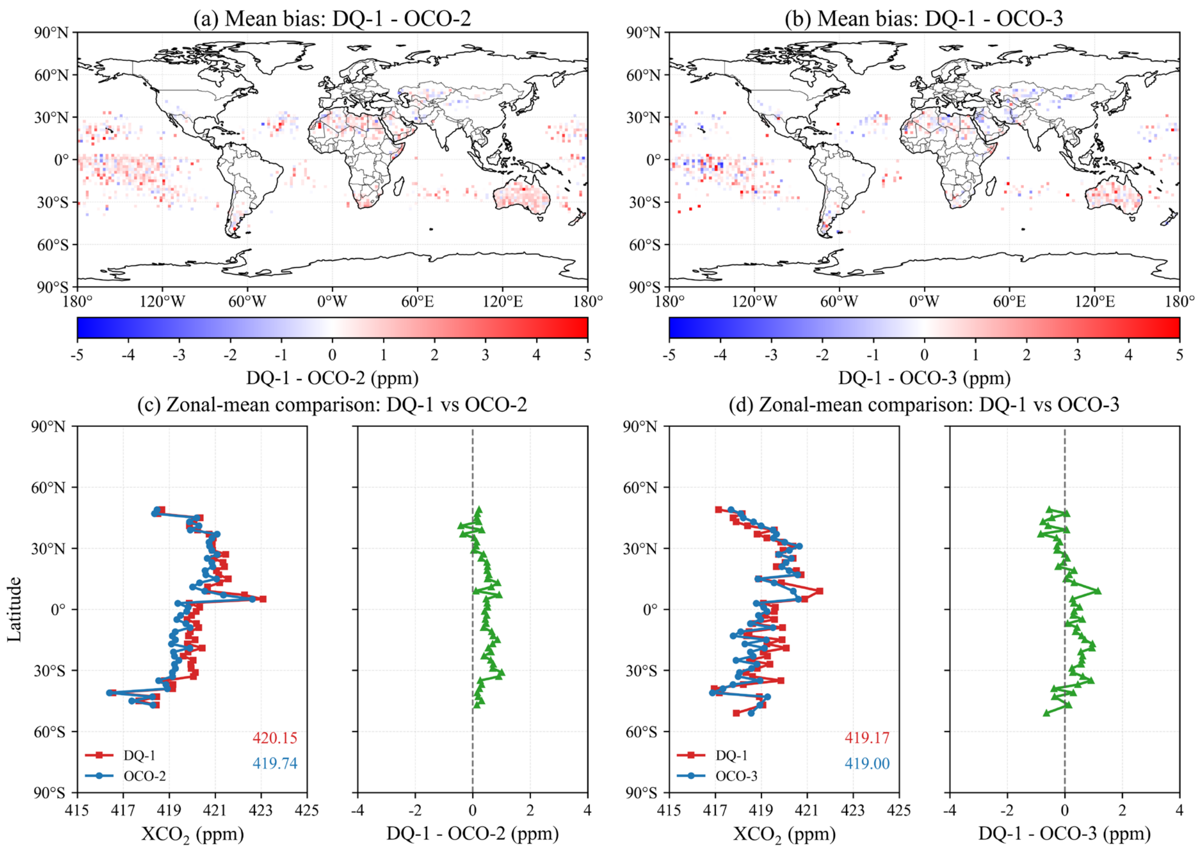

Figure 5. Spatial and zonal differences between DQ-1 and OCO-2/OCO-3 XCO_2 over the selected comparison regions. (a, b) Spatial distributions of the mean DQ-1–OCO-2 and DQ-1–OCO-3 differences, respectively. (c, d) Corresponding zonal-mean XCO_2 values and zonal-mean differences.

3.4.2 Relationships of DQ-1–OCO-2/OCO-3 XCO_2 BIAS and RMSE with MODIS reflectance

Figures 6 and 7 show, respectively, the relationships between MODIS Band 6 shortwave-infrared surface reflectance and the bias and RMSE of DQ-1 relative to OCO-2 and OCO-3. Spatially, MODIS reflectance is substantially higher over land than over ocean, especially in arid and semi-arid regions such as North Africa–the Middle East, Australia, and Central Asia, whereas ocean reflectance is generally low and has a narrower range. In contrast, the spatial distribution of bias is more heterogeneous, with positive and negative residuals spatially mixed and no clear correspondence with the reflectance field. The RMSE distribution also does not simply follow the regions of high reflectance. Higher RMSE values occur not only over some high-reflectance land areas and regions with complex surface conditions, but also over parts of the Southern Hemisphere oceans, the tropical Pacific, and coastal regions. These patterns suggest that the spatial characteristics of DQ-1–OCO-2/OCO-3 bias and RMSE cannot be explained by surface reflectance alone, and may also be related to ocean glint observation conditions and the distribution of valid collocated samples.

https://doi.org/10.5194/egusphere-2026-3864
Preprint. Discussion started: 17 July 2026

To further diagnose the influence of surface reflectance on the residuals, we calculate reflectance-binned statistics for the bias and RMSE of DQ-1–OCO-2 and DQ-1–OCO-3. For all samples, the linear relationship between bias and reflectance is weak, with correlation coefficients of approximately R = −0.22 for DQ-1–OCO-2 and R = −0.24 for DQ-1–OCO-3. This indicates that, when all samples are considered, reflectance is not the dominant factor controlling the mean bias. For samples over land, the DQ-1–OCO-2 bias increases slightly with reflectance, with R = 0.42, whereas the DQ-1–OCO-3 bias shows a weaker relationship with reflectance, with R = −0.21. For samples over ocean, the correlations are stronger, but the two comparison pairs show opposite trends: the DQ-1–OCO-2 bias increases with reflectance, with R = 0.77, whereas the DQ-1–OCO-3 bias decreases with reflectance, with R = −0.77. This indicates that the bias–reflectance relationship over ocean cannot be interpreted as a consistent reflectance-related tendency across the two comparison pairs.

RMSE shows a similar pattern. For all samples, the correlations between RMSE and reflectance are weak for both DQ-1–OCO-2 and DQ-1–OCO-3, with correlation coefficients of approximately R = −0.24 and R = −0.35, respectively. The correlations remain limited for samples over land, with R = −0.17 and R = −0.42, respectively. By contrast, the RMSE–reflectance relationships are more pronounced for samples over ocean, but again show opposite trends for the two comparison pairs: the RMSE of DQ-1–OCO-2 over ocean increases with reflectance, with R = 0.64, whereas that of DQ-1–OCO-3 decreases with reflectance, with R = −0.78. Because ocean reflectance has a relatively narrow range and the valid ocean samples are mainly obtained under glint observation conditions, these stronger correlations may reflect the combined variation in reflectance, ocean observation conditions, and sample distribution, rather than a direct dependence on reflectance itself. Overall, DQ-1–OCO-2/OCO-3 bias and RMSE do not show a consistent strong dependence on MODIS reflectance for all samples or for samples over land; the stronger but opposite correlations over ocean further indicate that the bias and RMSE over ocean cannot be explained by surface reflectance alone.

https://doi.org/10.5194/egusphere-2026-3864
Preprint. Discussion started: 17 July 2026

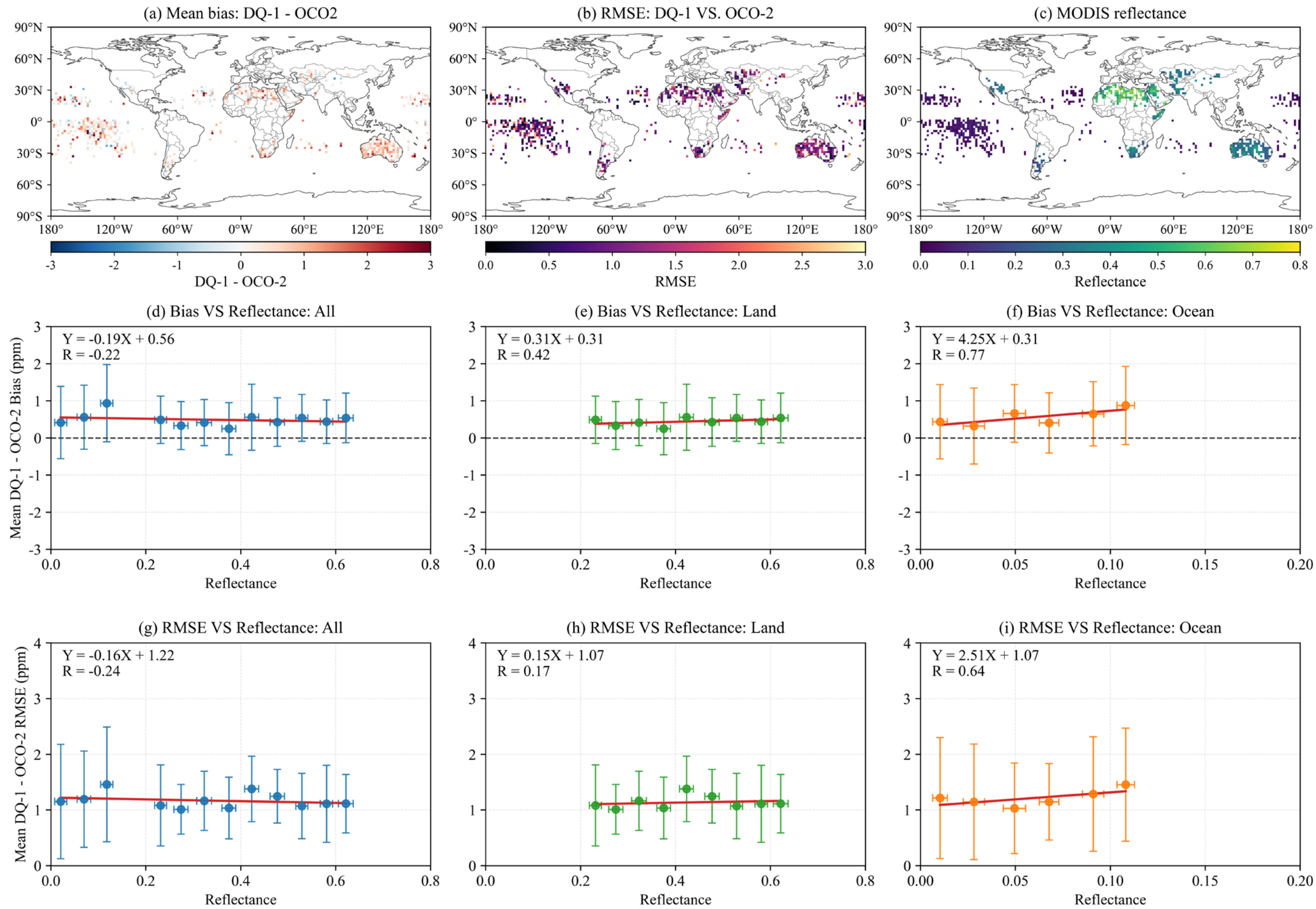

470 Figure 6. Spatial distributions and reflectance-binned statistics of DQ-1–OCO-2 XCO_2 residuals and MODIS Band 6 surface reflectance. (a–c) Spatial distributions of the mean DQ-1–OCO-2 bias, RMSE, and MODIS Band 6 reflectance, respectively. (d–f) Reflectance-binned mean bias for all, land, and ocean samples, respectively. (g–i) Corresponding reflectance-binned RMSE.

https://doi.org/10.5194/egusphere-2026-3864
Preprint. Discussion started: 17 July 2026

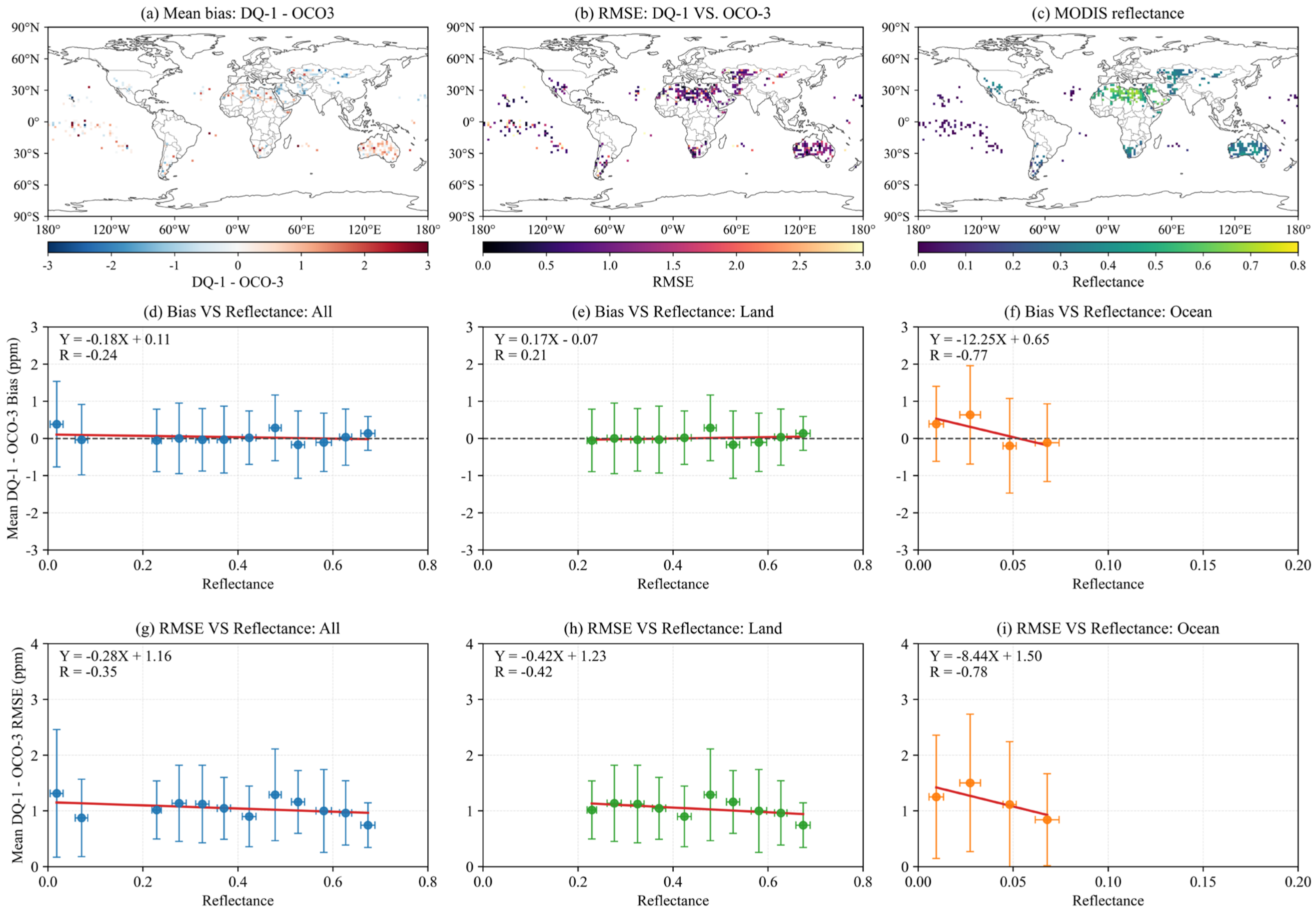

Figure 7. Spatial distributions and reflectance-binned statistics of DQ-1–OCO-3 XCO_2 residuals and MODIS Band 6 surface reflectance. (a–c) Spatial distributions of the mean DQ-1–OCO-3 bias, RMSE, and MODIS Band 6 reflectance, respectively. (d–f) Reflectance-binned mean bias for all, land, and ocean samples, respectively. (g–i) Corresponding reflectance-binned RMSE.

3.5 Nighttime DQ-1 XCO_2 compared with CAMS-derived XCO_2

Figure 8 shows the spatial distributions of nighttime DQ-1 XCO_2 and CAMS-derived XCO_2 under the DQ-1 column definition, together with the mean bias, RMSE, and zonal-mean comparisons. Their spatial distributions are generally consistent, with relatively high XCO_2 over low- and middle-latitude land regions in the Northern Hemisphere and lower XCO_2 over the Southern Hemisphere oceans and the tropical Pacific. The bias distribution indicates that the overall difference between DQ-1 and CAMS is small, with most grid cells within ±1 ppm and no clear global-scale positive or negative bias. Local positive biases are mainly found over North Africa and the Middle East, East Asia, and parts of the North Pacific,

https://doi.org/10.5194/egusphere-2026-3864
Preprint. Discussion started: 17 July 2026

whereas negative biases occur more frequently over the tropical Pacific, the Southern Hemisphere oceans, and regions near Australia.

The spatial distribution of RMSE shows that the differences are generally smaller over land, with most land grid cells below approximately 1.2 ppm. Higher RMSE values occur over the tropical Pacific, the Southern Hemisphere oceans, and some coastal regions, indicating relatively weaker consistency over the ocean. This may be related to surface-reflected shortwave-infrared signals over oceans, cloud/aerosol filtering, and differences in the distribution of valid samples (Boesch et al., 2011; Crisp et al., 2017; Wunch et al., 2017), and may also be affected by uncertainties in the CAMS CO_2 profiles.

The zonal-mean comparisons show consistent latitudinal variations between DQ-1 and CAMS. For all samples, the mean XCO_2 values of DQ-1 and CAMS are 419.67 and 419.61 ppm, respectively. The corresponding values are 419.76 and 419.71 ppm over land, and 419.48 and 419.45 ppm over ocean. The mean differences are therefore smaller than 0.1 ppm for all three sample groups. The scatterplots further show a strong linear relationship between nighttime DQ-1 XCO_2 and CAMS-derived XCO_2 for daily 2° paired samples (Fig. A2). For all samples, R = 0.91, mean bias = 0.04 ppm, and RMSE = 1.33 ppm. The land samples show better agreement, with R = 0.93 and RMSE = 1.18 ppm, whereas the ocean samples show larger scatter, with R = 0.87 and RMSE = 1.50 ppm. Overall, nighttime DQ-1 XCO_2 is broadly consistent with CAMS-derived XCO_2 in terms of spatial distribution, zonal variation, and daily 2° paired statistics, indicating good consistency with the CAMS-derived XCO_2 reference field.

https://doi.org/10.5194/egusphere-2026-3864
Preprint. Discussion started: 17 July 2026

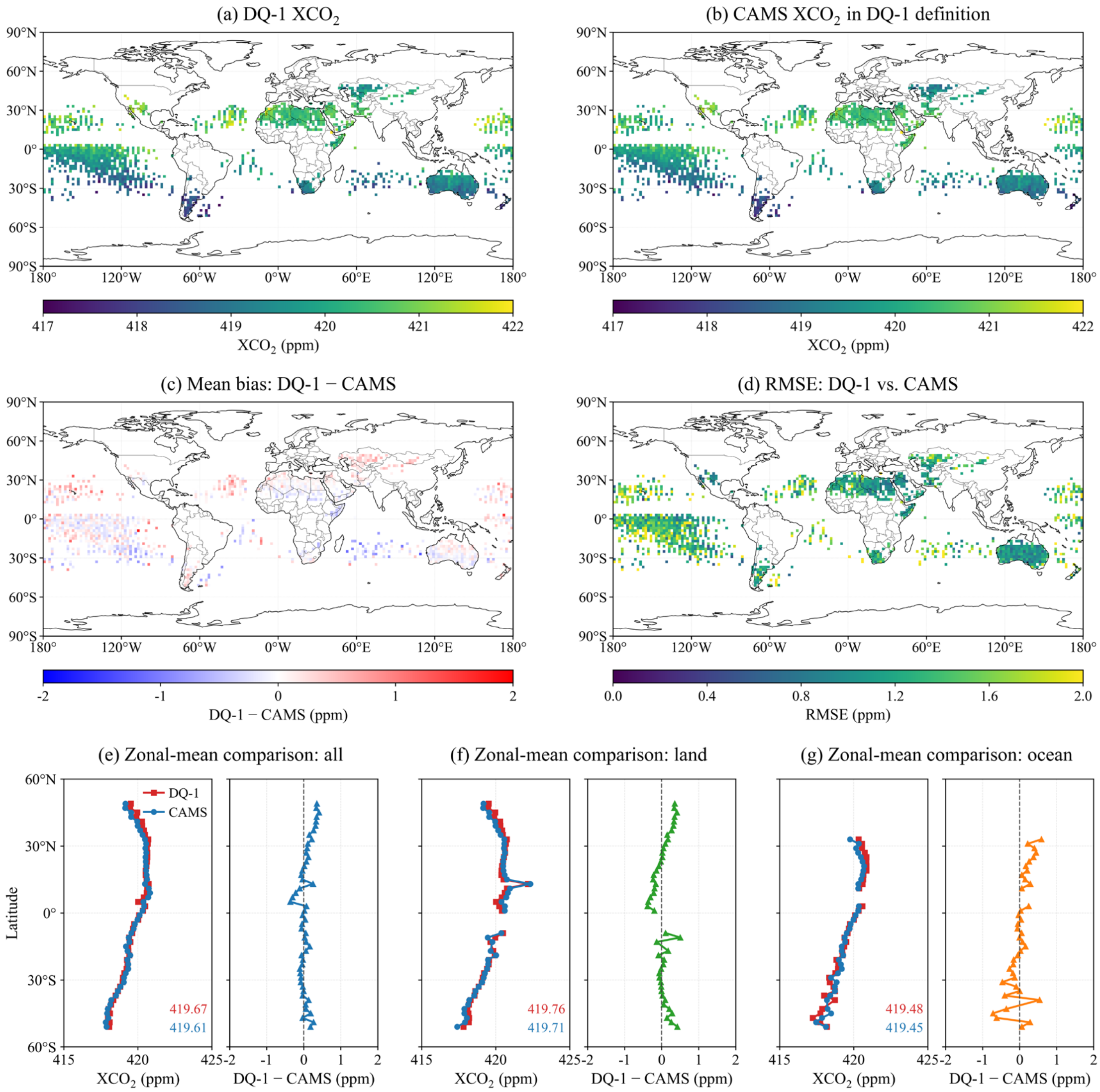

Figure 8. Spatial, residual, and zonal comparisons between nighttime DQ-1 XCO_2 and CAMS-derived XCO_2 under the DQ-1 column definition. (a, b) Spatial distributions of nighttime DQ-1 XCO_2 and CAMS-derived XCO_2, respectively. (c, d) Spatial distributions of the mean bias and RMSE. (e–g) Zonal-mean comparisons for all, land, and ocean samples.

3.6 Monthly regional XCO_2 comparisons in representative regions

Figure 9 shows the monthly regional mean XCO_2 variations of DQ-1, OCO-2, OCO-3, GOSAT, and GOSAT-2 in ten representative regions from June 2022 to December 2024. Overall, the five regions in the left column, namely Western America, North Atlantic, Sahara, Equatorial Pacific, and Australia, show relatively good consistency among the satellite products. Except for GOSAT-2, DQ-1, OCO-2, OCO-3, and GOSAT consistently capture the seasonal variability and overall increase

https://doi.org/10.5194/egusphere-2026-3864
Preprint. Discussion started: 17 July 2026

in regional XCO_2. In these five regions, the regional mean XCO_2 values of these four products are approximately 419.9–420.8, 419.3–420.8, 418.5–420.5, 418.4–419.7, and 417.3–419.1 ppm, respectively. This indicates that, in regions with relatively stable background conditions and sufficient multi-satellite sampling, DQ-1 active observations are comparable to passive optical XCO_2 products at the monthly regional scale.

Notably, GOSAT-2 is systematically higher than the other satellite products in most regions. In the five relatively stable regions mentioned above, the mean XCO_2 of GOSAT-2 is generally about 3.2–3.6 ppm higher than the mean of the other four products. Similar positive biases are also found in China, India, and the Amazon. This result is consistent with the pairwise comparisons in Sect. 3.3 and further indicates that the GOSAT-2 product used in this study exhibits a systematic positive bias at the regional monthly scale.

The five regions in the right column more clearly highlight the complementary role of DQ-1 relative to passive satellite observations. Passive NIR/SWIR products provide fewer valid monthly XCO_2 values in regions such as the Boreal Forest, India, the Amazon, and Antarctica. This may be associated with the combined effects of high aerosol loading, cloud contamination, complex surface conditions, observation geometry, and high-latitude solar-illumination limitations. For OCO-3, the reduced coverage partly reflects its ISS-related stowage and reconfiguration period, as noted in Sect. 3.1. Using the criterion that a monthly regional mean is valid only when at least 5 valid observation days are available in that month, DQ-1 provides valid monthly means for all 31 months in all ten regions. In contrast, OCO-3 has no valid monthly means in the Boreal Forest and Antarctica, and only 20 and 22 valid months in India and the Amazon, respectively. The contrast is most evident in Antarctica: DQ-1 provides valid monthly means for all 31 months during the study period, whereas OCO-2 has only 10 valid months, OCO-3 and GOSAT have no valid monthly means, and GOSAT-2 has only 2 valid months.

These results indicate that DQ-1 does not merely duplicate existing passive satellite observations, but provides more continuous complementary XCO_2 observational coverage in high-aerosol, high-latitude, and passive-observation-limited regions. This finding is consistent with Han et al. (2024), who showed that ACDL/DQ-1 can acquire XCO_2 observations under nighttime, high-aerosol, and high-latitude conditions, suggesting that active IPDA observations can provide an effective complement when passive NIR/SWIR observations are limited.

https://doi.org/10.5194/egusphere-2026-3864
Preprint. Discussion started: 17 July 2026

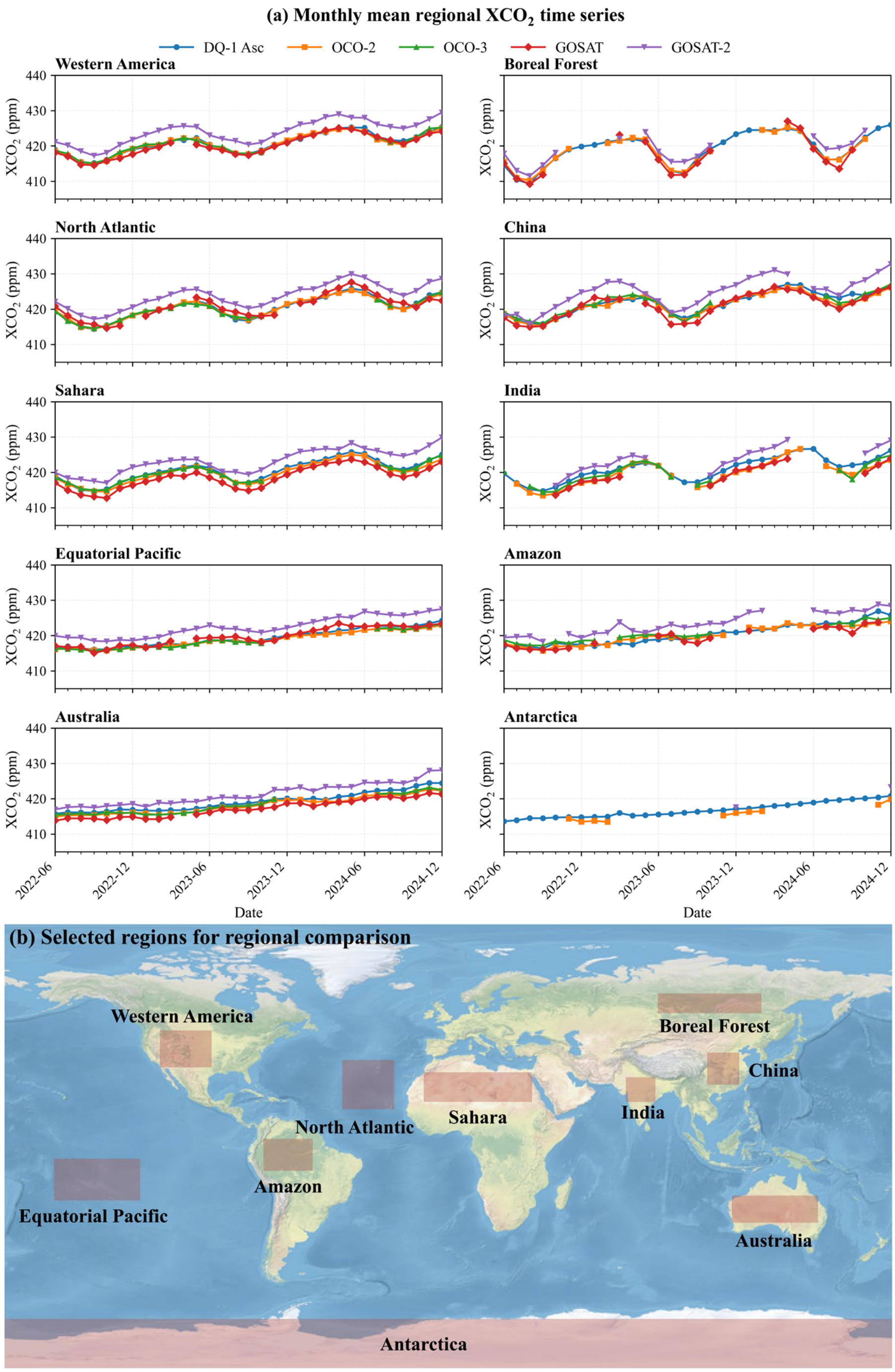

Figure 9. Monthly regional mean XCO_2 time series for selected representative regions and their locations. (a) Monthly mean regional XCO_2 time series from DQ-1, OCO-2, OCO-3, GOSAT, and GOSAT-2. (b) Locations of the ten selected regions used for regional comparison.

https://doi.org/10.5194/egusphere-2026-3864
Preprint. Discussion started: 17 July 2026

3.7 Independent validation with TCCON observations

We further use TCCON observations to evaluate the external consistency of DQ-1 and passive satellite XCO_2 products. Figure 10 shows that OCO-2 and OCO-3 have the strongest agreement with TCCON, with correlation coefficients of $R = 0.95$ and 0.94, mean biases of −0.18 and 0.08 ppm, and RMSE values of 1.09 and 1.12 ppm, respectively. These results indicate small systematic biases and random scatter for the OCO products, consistent with the validation results for OCO-2 and OCO-3 reported by Taylor et al. (2023). GOSAT also agrees well with TCCON, with $R = 0.91$, a mean bias of −0.28 ppm, and an RMSE of 1.45 ppm. Although its scatter is larger than that of OCO-2 and OCO-3, its overall bias remains small.

In contrast, GOSAT-2 still shows a high correlation with TCCON $R = 0.91$, but has a mean bias of 3.56 ppm and an RMSE of 3.98 ppm, indicating a pronounced positive bias. Similar behavior has also been reported in previous evaluation studies. Yang et al. (2025) found that monthly mean GOSAT-2 XCO_2 was about 2 ppm higher than those from GOSAT, OCO-2, and OCO-3, with BIAS and RMSE relative to TCCON of 2.42 and 3.16 ppm, respectively. Ji et al. (2024) also reported significant overestimation by GOSAT-2 at East Asian TCCON sites, with an ME of 2.95 ppm. Notably, Yoshida et al. (2023) stated that the GOSAT-2 SWIR L2 product provides XCO_2 retrievals that have not been empirically bias corrected and require further correction using empirical bias-correction equations. Therefore, the positive bias of GOSAT-2 relative to TCCON in this study is likely related mainly to the lack of bias correction, although differences in product version and retrieval algorithm may also contribute.

The comparison between DQ-1 and TCCON shows that, although the number of valid collocations is smaller than that for the passive satellites, DQ-1 still has $R = 0.92$, a mean bias of 0.21 ppm, and an RMSE of 1.49 ppm. These statistics are comparable to that of GOSAT, slightly higher than those of OCO-2 and OCO-3, and much lower than that of GOSAT-2, indicating that daytime DQ-1 ACDL XCO_2 is consistent with TCCON observations. This result is consistent with the initial validation of ACDL XCO_2 by Han et al. (2025), who reported a near-zero mean bias and an RMSE of about 1.4 ppm. The relatively limited number of DQ-1–TCCON collocations is mainly constrained by the point-sampling geometry of the active lidar observations. Unlike passive sensors with wider swaths or denser sampling, DQ-1/ACDL samples only along its ground track, which reduces the probability of close spatiotemporal coincidence with TCCON sites. Overall, the independent TCCON validation shows that daytime DQ-1 XCO_2 has external consistency comparable to passive satellite products, supporting its role as an important complement to passive satellite XCO_2 observations.

https://doi.org/10.5194/egusphere-2026-3864
Preprint. Discussion started: 17 July 2026

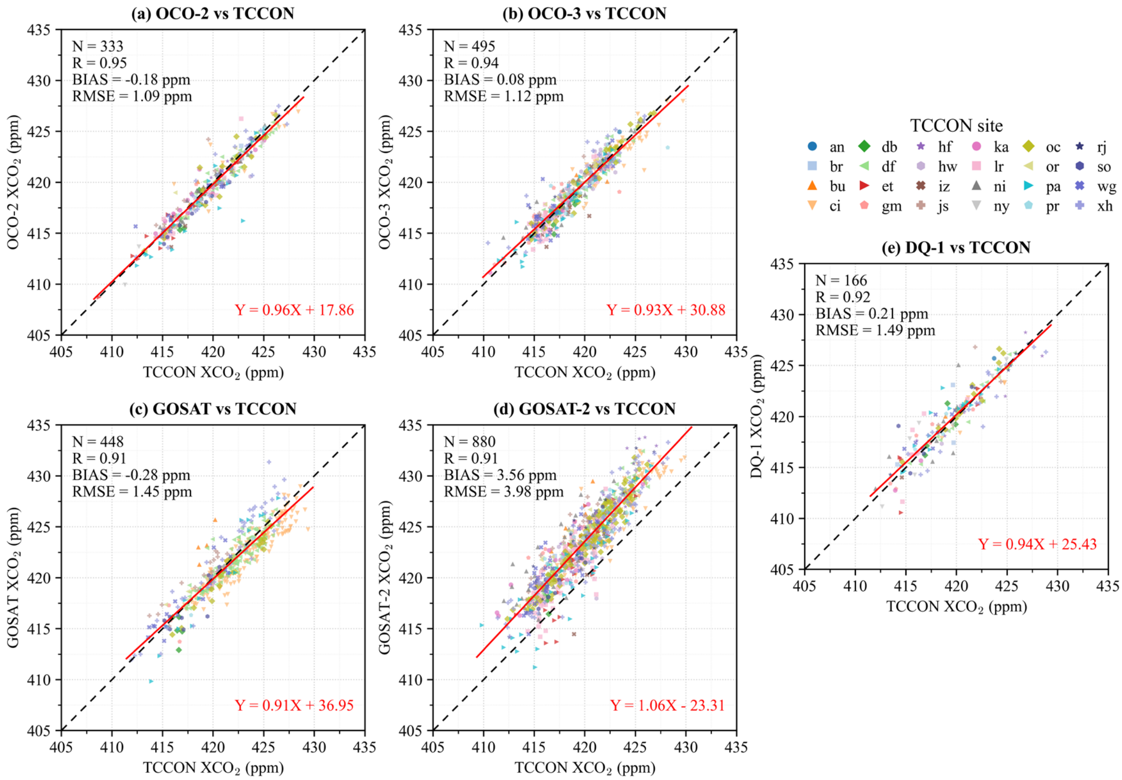

Figure 10. Independent validation of satellite XCO_2 products against TCCON observations. (a–e) Paired comparisons of OCO-2, OCO-3, GOSAT, GOSAT-2, and DQ-1 XCO_2 against TCCON XCO_2, respectively. Different colors and symbols represent different TCCON sites. The red lines indicate linear least-squares fits, and the black dashed lines indicate the 1:1 lines.

4 Discussion

4.1 Performance and complementary role of DQ-1 ACDL in satellite XCO_2 observations

The inter-satellite comparisons, TCCON validation, and nighttime model-reference diagnosis together indicate that DQ-1 ACDL has the consistency required to contribute to a multi-source satellite XCO_2 observing system. DQ-1 shows small mean differences relative to OCO-2 and OCO-3, remains consistent with passive optical satellite products in large-scale spatial distributions, meridional structures, and regional monthly variations, and shows daytime TCCON validation performance comparable to that of GOSAT. These results support the use of DQ-1 ACDL as a quantitatively comparable active component of the existing passive optical XCO_2 observing system.

The main value of DQ-1 is not to replace passive optical satellites, but to provide complementary XCO_2 observational coverage under conditions where passive NIR/SWIR retrievals are limited. These include nighttime observations, high-latitude regions, cloud- and aerosol-affected scenes, complex surface conditions, and periods with limited solar illumination. This complementary observing capability can improve the spatiotemporal continuity of satellite greenhouse gas observations and

https://doi.org/10.5194/egusphere-2026-3864
Preprint. Discussion started: 17 July 2026

provide additional support for future active–passive joint XCO_2 constraints, regional carbon flux inversions, and emission monitoring.

4.2 Limitations of the comparison framework

The results should be interpreted within the limitations of the unified comparison framework. First, CAMS CO_2 fields are used for coherent-region selection, estimation of XCO_2 column-definition differences, and nighttime DQ-1 XCO_2 diagnosis. Therefore, the reported differences should be regarded as consistency between satellite products after model-assisted correction for XCO_2 column-definition differences, rather than as a fully model-independent assessment of absolute errors. In addition, daily 2° aggregation and the 4 h temporal matching criterion reduce footprint-scale noise and sampling imbalance, but may smooth real XCO_2 gradients in strong-emission regions, land–ocean transition zones, complex terrain, and regions affected by rapidly changing transport.

Further uncertainties arise from differences in retrieval algorithms, quality filtering, product versions, and bias-correction status among the satellite products. The positive bias found for the GOSAT-2 product used in this study indicates that inter-product biases should be explicitly considered before multi-source XCO_2 products are jointly used. Finally, because TCCON provides an independent reference only for daytime satellite observations, the nighttime DQ-1 comparison with CAMS-derived XCO_2 should be interpreted as a comparison relative to an external model reference, rather than as an independent observational validation.

Conclusions

In this study, we compared DQ-1 ACDL XCO_2 with passive optical satellite XCO_2 products from OCO-2, OCO-3, GOSAT, and GOSAT-2 from June 2022 to December 2024. The comparison was conducted within a unified framework that combines CAMS-based spatiotemporal coherence screening, multi-satellite sampling availability, daily 2° aggregation, spatiotemporal collocation, and correction for XCO_2 column-definition differences. By reducing the influence of sampling representativeness and observation-operator differences, this framework provides a common basis for interpreting inter-product XCO_2 differences.

The results show that DQ-1 ACDL is broadly consistent with OCO-2 and OCO-3 over coherent and well-sampled comparison regions. The mean DQ-1–OCO-2/OCO-3 differences are generally below 0.5 ppm, and the products show similar large-scale spatial distributions, meridional structures, and regional monthly variations. Independent validation against TCCON shows that daytime DQ-1 XCO_2 has a correlation coefficient of 0.92, a mean bias of 0.21 ppm, and an RMSE of 1.49 ppm, with validation statistics comparable to those of GOSAT. The nighttime comparison further shows that, under the DQ-1 column definition, DQ-1 XCO_2 is broadly consistent with CAMS-derived XCO_2. In contrast, the GOSAT-2 product used in this study shows a clear positive bias in both the inter-satellite comparisons and the TCCON validation, emphasizing the importance of bias-correction status in multi-satellite XCO_2 applications. The MODIS Band 6 diagnosis also indicates that DQ-1–OCO-2/OCO-3 bias and RMSE do not show a consistent strong dependence on surface reflectance; the stronger but

https://doi.org/10.5194/egusphere-2026-3864
Preprint. Discussion started: 17 July 2026

opposite relationships over ocean likely reflect combined effects of reflectance, glint-viewing conditions, and collocated-sample distributions.

Compared with previous studies that mainly evaluated individual XCO_2 products or intercomparisons among passive satellites, this study establishes a unified method for assessing the consistency between DQ-1 active IPDA lidar and passive XCO_2 products. After applying common sampling, aggregation, collocation, and column-definition treatment, the small differences between DQ-1 and OCO-2/OCO-3 indicate that DQ-1 ACDL XCO_2 is quantitatively comparable to mature passive optical satellite products in the selected comparison regions. These results should still be interpreted within the limits of the comparison framework. CAMS CO_2 fields are used for comparison-region selection, column-definition correction, and nighttime DQ-1 diagnosis; therefore, the reported differences should be regarded as product-level consistency after model-assisted treatment of column-definition differences, rather than as a fully model-independent assessment of absolute retrieval errors. In addition, daily 2° aggregation and the 4 h temporal matching criterion reduce sampling noise but may smooth real XCO_2 gradients in strong-emission regions, land–ocean transition zones, complex terrain, and rapidly changing transport conditions. Because independent nighttime TCCON or passive NIR/SWIR XCO_2 observations are not available, the nighttime DQ-1 result should be interpreted as a comparison with an external model reference.

Overall, DQ-1 ACDL provides an important active XCO_2 observational capability for the satellite CO_2 observing system. Its consistency with OCO-2, OCO-3, GOSAT, and TCCON indicates that DQ-1 ACDL can provide XCO_2 observations with validation performance and product-level consistency comparable to established passive products. More importantly, DQ-1 can extend satellite CO_2 sampling to conditions where passive NIR/SWIR observations are limited, including nighttime, high-latitude regions, aerosol- or cloud-affected scenes, complex surface conditions, unfavorable viewing geometry, and periods with weak solar illumination. These capabilities can improve the spatiotemporal continuity of atmospheric CO_2 observations and provide additional constraints for future active–passive joint XCO_2 analyses, regional carbon flux inversions, carbon-cycle studies, and emission-monitoring applications. Future work should extend active–passive XCO_2 comparisons at higher spatiotemporal resolution and under different observing conditions to better quantify the complementarity between DQ-1 and passive XCO_2 products. At the application level, active–passive joint assimilation and flux inversion are needed to quantify the potential improvement that combined XCO_2 constraints can provide in estimates of regional carbon fluxes and anthropogenic emissions.

https://doi.org/10.5194/egusphere-2026-3864
Preprint. Discussion started: 17 July 2026

Appendix A

Table A1. Abbreviated names, geographic information, and valid observation periods of the TCCON sites used for validation.

Abbreviated name	TCCON site	Latitude(°N)	Longitude(°E)	Altitude(m)
an	Anmyeondo [anmeyondo01]	36.54	126.33	20
br	Bremen [bremen01]	53.10	8.85	30
bu	Burgos [burgos01]	18.53	120.65	40
ci	Caltech [pasadena01]	34.14	−118.13	240
db	Darwin [darwin01]	-12.46	130.93	40
df	Edwards [edwards01]	34.96	−117.88	700
et	East Trout Lake [easttroutlake01]	54.35	−104.99	502
gm	Garmisch [garmisch01]	47.48	11.06	743
hf	Hefei [hefei01]	31.91	117.17	40
hw	Harwell [harwell01]	51.57	−1.32	142
iz	Izana [izana01]	28.31	−16.50	2370
js	Saga [saga01]	33.24	130.29	9
ka	Karlsruhe [karlsruhe01]	49.10	8.44	110
lr	Lauder [lauder03]	-45.04	169.68	370
ni	Nicosia [nicosia01]	35.14	33.38	185
ny	Ny-Ålesund [nyalesund01]	78.92	11.92	20
oc	Lamont [lamont01]	36.60	−97.49	320
or	Orléans [orleans01]	47.96	2.11	130
pa	Park Falls [parkfalls01]	45.94	−90.27	476
pr	Paris [paris01]	48.85	2.36	60
rj	Rikubetsu [rikubetsu01]	43.46	143.77	380
so	Sodankylä [sodankyla01]	67.37	26.63	188
wg	Wollongong [wollongong01]	-34.41	150.88	30
xh	Xianghe [xianghe01]	39.80	116.96	40

https://doi.org/10.5194/egusphere-2026-3864
Preprint. Discussion started: 17 July 2026

Table A2. Pairwise consistency statistics for the satellite XCO_2 products over the selected comparison regions.

Y-axis product	X-axis product	Surface type	N	R	Bias (ppm)	RMSE (ppm)	Slope	Intercept (ppm)
DQ-1	OCO-2	Land	1559	0.93	0.45	1.27	0.97	12.53
		Ocean	1922	0.89	0.49	1.59	1.03	-11.32
DQ-1	OCO-3	Land	1099	0.92	0.06	1.26	0.96	15.01
		Ocean	629	0.86	0.39	1.74	1.03	-10.23
DQ-1	GOSAT	Land	80	0.90	0.76	1.47	0.84	65.72
		Ocean	79	0.76	-1.39	2.30	0.79	87.52
DQ-1	GOSAT-2	Land	569	0.87	-2.66	3.19	0.70	122.79
		Ocean	479	0.82	-3.36	3.84	0.79	87.05
OCO-2	OCO-3	Land	1435	0.97	-0.30	0.81	0.95	21.73
		Ocean	1203	0.99	-0.08	0.45	0.96	17.93
OCO-2	GOSAT	Land	86	0.94	0.08	1.03	0.88	51.58
		Ocean	96	0.94	-1.34	1.66	0.82	74.62
OCO-2	GOSAT-2	Land	754	0.91	-3.48	3.82	0.68	129.65
		Ocean	667	0.94	-3.75	3.97	0.73	108.59
OCO-3	GOSAT	Land	63	0.91	0.76	1.38	0.96	15.52
		Ocean	49	0.93	-1.27	1.64	0.81	78.34
OCO-3	GOSAT-2	Land	534	0.93	-2.90	3.29	0.70	122.60
		Ocean	307	0.92	-3.70	3.97	0.71	118.00
GOSAT-2	GOSAT	Land	122	0.88	4.68	4.94	1.06	-19.95
		Ocean	61	0.95	2.79	2.99	1.02	-7.58

https://doi.org/10.5194/egusphere-2026-3864
Preprint. Discussion started: 17 July 2026

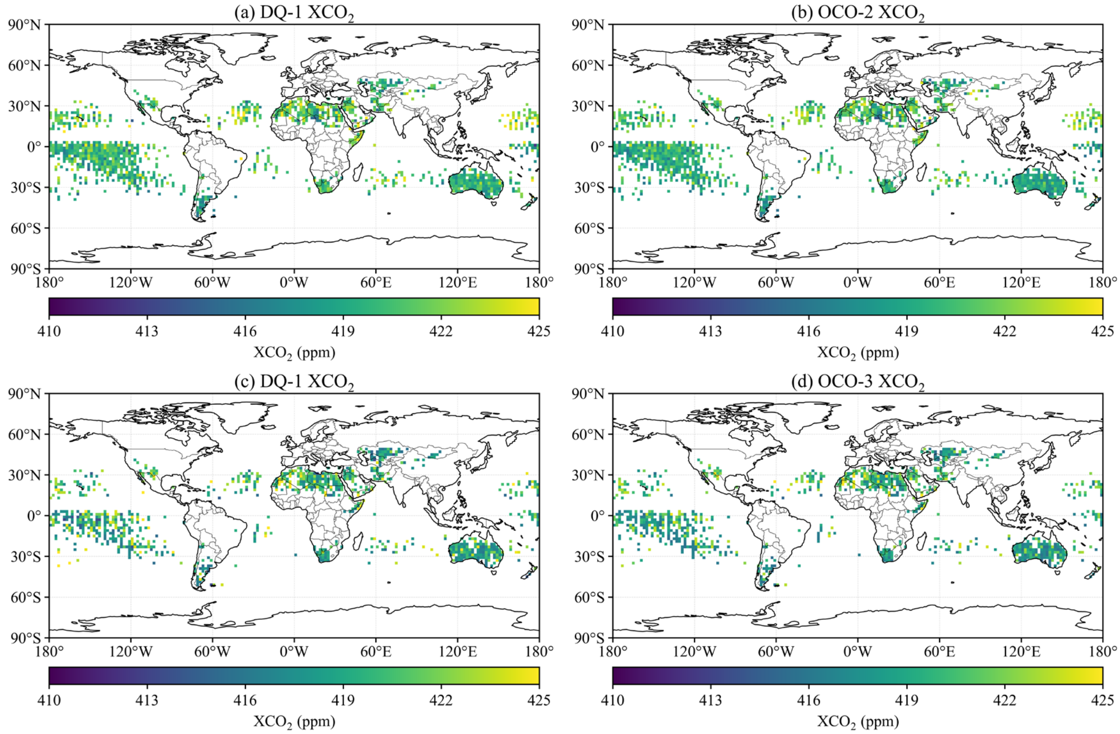

Figure A1. Spatial distributions of paired DQ-1, OCO-2, and OCO-3 XCO₂ samples over the selected 2° comparison grid cells.

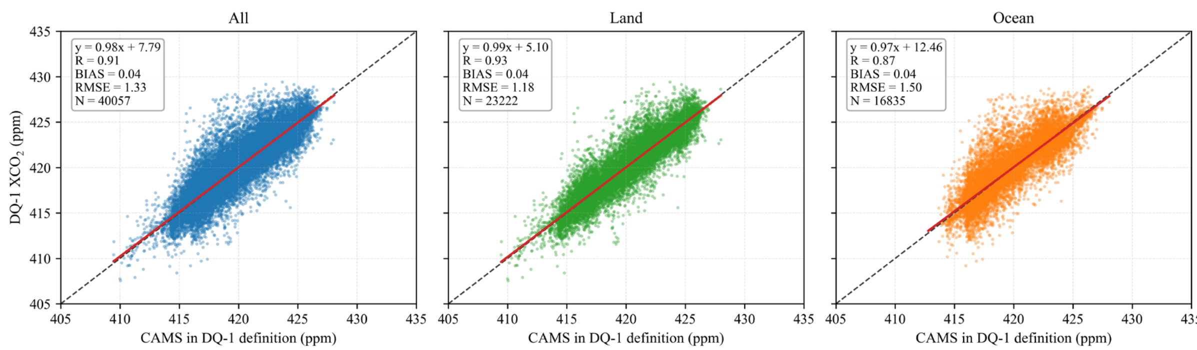

Figure A2. Scatterplot comparison between nighttime DQ-1 XCO₂ and CAMS-derived XCO₂ for daily 2° paired samples under the DQ-1 column definition.

Data availability

The DQ-1 ACDL XCO₂ products underlying the results presented in this paper are not publicly available at this time because of data-distribution restrictions, but may be obtained from the corresponding author upon reasonable request. The OCO-2 L2 Lite XCO₂ product (OCO2_L2_Lite_FP, v11.2r) and OCO-3 L2 Lite XCO₂ product (OCO3_L2_Lite_FP, v11r) are available under the DOIs https://doi.org/10.5067/70K2B2W8MNGY and https://doi.org/10.5067/8U0VGVQC7HZG,

https://doi.org/10.5194/egusphere-2026-3864
Preprint. Discussion started: 17 July 2026

respectively. The GOSAT SWIR L2 XCO_2 product is available from the GOSAT Data Archive Service (https://data2.gosat.nies.go.jp/index_en.html, last access: 20 June 2026). The GOSAT-2 SWIR L2 XCO_2 product is available from the GOSAT-2 Product Archive (https://prdct.gosat-2.nies.go.jp/aboutdata/howtoaccessdata.html, last access: 20 June 2026). The CAMS global greenhouse gas inversion-optimized CO_2 data are available from the Copernicus Atmosphere Data Store (https://ads.atmosphere.copernicus.eu/datasets/cams-global-greenhouse-gas-inversion?tab=overview, last access: 20 June 2026). The Aqua MODIS MYD09CMG.061 surface reflectance product is available under the DOI https://doi.org/10.5067/MODIS/MYD09CMG.061. The TCCON GGG2020 ground-based XCO_2 data are available under the DOI https://doi.org/10.14291/TCCON.GGG2020. All publicly available datasets were used in accordance with the data policies and citation requirements of the respective data providers.

Author contributions

Author contributions. The study was designed by GH and YW. Data collection and processing were carried out by YW, YH, HZ, KZ, and GH. YW performed the main data analysis and wrote the manuscript. HZ, YH, and KZ contributed to data analysis and result interpretation. WG and GH provided funding. All authors reviewed, commented on, and approved the manuscript.

Competing interests

The contact author has declared that none of the authors has any competing interests.

Disclaimer

Publisher's note: Copernicus Publications remains neutral with regard to jurisdictional claims made in the text, published maps, institutional affiliations, or any other geographical representation in this paper. The authors bear the ultimate responsibility for providing appropriate place names. Views expressed in the text are those of the authors and do not necessarily reflect the views of the publisher.

Acknowledgements

The authors thank all the financial support for this research. This research was supported by the National Natural Science Foundation of China (grant-no.: 42475144), National Key R&D Program of China (grant-no.: 2024YFB3910203), and Beijing Natural Science Foundation (grant-no.: L211045).

Financial support

This research has been supported by the National Natural Science Foundation of China (grant no. 42475144) and the Fundamental Research Funds for the Central Universities (grant-no. 2042025kf0036).

https://doi.org/10.5194/egusphere-2026-3864
Preprint. Discussion started: 17 July 2026

References

Abshire, J., Ramanathan, A., Riris, H., Mao, J., Allan, G., Hasselbrack, W., Weaver, C., and Browell, E.: Airborne Measurements of CO2 Column Concentration and Range Using a Pulsed Direct-Detection IPDA Lidar, Remote Sensing, 6, 443-469, https://doi.org/10.3390/rs6010443, 2014.

Abshire, J., Riris, H., Allan, G., Weaver, C., Mao, J., Sun, X., Hasselbrack, W., Kawa, S. R., and Biraud, S.: Pulsed airborne lidar measurements of atmospheric CO2 column absorption, Tellus B: Chemical and Physical Meteorology, 62, 770, https://doi.org/10.1111/j.1600-0889.2010.00502.x, 2010.

Amediek, A., Ehret, G., Fix, A., Wirth, M., Büdenbender, C., Quatrevalet, M., Kiemle, C., and Gerbig, C.: CHARM-F—a new airborne integrated-path differential-absorption lidar for carbon dioxide and methane observations: measurement performance and quantification of strong point source emissions, Applied Optics, 56, 5182, https://doi.org/10.1364/ao.56.005182, 2017.

Basu, S., Baker, D. F., Chevallier, F., Patra, P. K., Liu, J., and Miller, J. B.: The impact of transport model differences on CO2 surface flux estimates from OCO-2 retrievals of column average CO2, Atmospheric Chemistry and Physics, 18, 7189-7215, https://doi.org/10.5194/acp-18-7189-2018, 2018.

Boesch, H., Baker, D., Connor, B., Crisp, D., and Miller, C.: Global Characterization of CO2 Column Retrievals from Shortwave-Infrared Satellite Observations of the Orbiting Carbon Observatory-2 Mission, Remote Sensing, 3, 270-304, https://doi.org/10.3390/rs3020270, 2011.

Buchwitz, M., de Beek, R., Burrows, J. P., Bovensmann, H., Warneke, T., Notholt, J., Meirink, J. F., Goede, A. P. H., Bergamaschi, P., Körner, S., Heimann, M., and Schulz, A.: Atmospheric methane and carbon dioxide from SCIAMACHY satellite data: initial comparison with chemistry and transport models, Atmospheric Chemistry and Physics, 5, 941-962, https://doi.org/10.5194/acp-5-941-2005, 2005.

Buchwitz, M., Reuter, M., Schneising, O., Hewson, W., Detmers, R. G., Boesch, H., Hasekamp, O. P., Aben, I., Bovensmann, H., Burrows, J. P., Butz, A., Chevallier, F., Dils, B., Frankenberg, C., Heymann, J., Lichtenberg, G., De Mazière, M., Notholt, J., Parker, R., Warneke, T., Zehner, C., Griffith, D. W. T., Deutscher, N. M., Kuze, A., Suto, H., and Wunch, D.: Global satellite observations of column-averaged carbon dioxide and methane: The GHG-CCI XCO2 and XCH4 CRDP3 data set, Remote Sensing of Environment, 203, 276-295, https://doi.org/10.1016/j.rse.2016.12.027, 2017.

Chevallier, F., Engelen, R. J., and Peylin, P.: The contribution of AIRS data to the estimation of CO2 sources and sinks, Geophysical Research Letters, 32, 2005GL024229, https://doi.org/10.1029/2005gl024229, 2005.

Chevallier, F., Ciais, P., Conway, T. J., Aalto, T., Anderson, B. E., Bousquet, P., Brunke, E. G., Ciattaglia, L., Esaki, Y., Fröhlich, M., Gomez, A., Gomez-Pelaez, A. J., Haszpra, L., Krummel, P. B., Langenfelds, R. L., Leuenberger, M., Machida, T., Maignan, F., Matsueda, H., Morguí, J. A., Mukai, H., Nakazawa, T., Peylin, P., Ramonet, M., Rivier, L., Sawa, Y., Schmidt, M., Steele, L. P., Vay, S. A., Vermeulen, A. T., Wofsy, S., and Worthy, D.: CO2 surface fluxes at

https://doi.org/10.5194/egusphere-2026-3864
Preprint. Discussion started: 17 July 2026

grid point scale estimated from a global 21 year reanalysis of atmospheric measurements, Journal of Geophysical Research: Atmospheres, 115, 2010JD013887, https://doi.org/10.1029/2010jd013887, 2010.

Crisp, D., Pollock, H. R., Rosenberg, R., Chapsky, L., Lee, R. A. M., Oyafuso, F. A., Frankenberg, C., O'Dell, C. W., Bruegge, C. J., Doran, G. B., Eldering, A., Fisher, B. M., Fu, D., Gunson, M. R., Mandrake, L., Osterman, G. B., Schwandner, F. M., Sun, K., Taylor, T. E., Wennberg, P. O., and Wunch, D.: The on-orbit performance of the Orbiting Carbon Observatory-2 (OCO-2) instrument and its radiometrically calibrated products, Atmospheric Measurement Techniques, 10, 59-81, https://doi.org/10.5194/amt-10-59-2017, 2017.

Crowell, S. M. R., Randolph Kawa, S., Browell, E. V., Hammerling, D. M., Moore, B., Schaefer, K., and Doney, S. C.: On the Ability of Space-Based Passive and Active Remote Sensing Observations of CO2 to Detect Flux Perturbations to the Carbon Cycle, Journal of Geophysical Research: Atmospheres, 123, 1460-1477, https://doi.org/10.1002/2017jd027836, 2018.

Eldering, A., O'Dell, C. W., Wennberg, P. O., Crisp, D., Gunson, M. R., Viatte, C., Avis, C., Braverman, A., Castano, R., Chang, A., Chapsky, L., Cheng, C., Connor, B., Dang, L., Doran, G., Fisher, B., Frankenberg, C., Fu, D., Granat, R., Hobbs, J., Lee, R. A. M., Mandrake, L., McDuffie, J., Miller, C. E., Myers, V., Natraj, V., O'Brien, D., Osterman, G. B., Oyafuso, F., Payne, V. H., Pollock, H. R., Polonsky, I., Roehl, C. M., Rosenberg, R., Schwandner, F., Smyth, M., Tang, V., Taylor, T. E., To, C., Wunch, D., and Yoshimizu, J.: The Orbiting Carbon Observatory-2: first 18 months of science data products, Atmospheric Measurement Techniques, 10, 549-563, https://doi.org/10.5194/amt-10-549-2017, 2017.

Fang, J., Chen, B., Zhang, H., Dilawar, A., Guo, M., Liu, C., Liu, S. a., Gemechu, T. M., and Zhang, X.: Global Evaluation and Intercomparison of XCO2 Retrievals from GOSAT, OCO-2, and TANSAT with TCCON, Remote Sensing, 15, 5073, https://doi.org/10.3390/rs15205073, 2023.

Friedlingstein, P., O'Sullivan, M., Jones, M. W., Andrew, R. M., Bakker, D. C. E., Hauck, J., Landschützer, P., Le Quéré, C., Li, H., Luijkx, I. T., Peters, G. P., Peters, W., Pongratz, J., Schwingshackl, C., Sitch, S., Canadell, J. G., Ciais, P., Aas, K., Alin, S. R., Anthoni, P., Barbero, L., Bates, N. R., Bellouin, N., Benoit-Cattin, A., Berghoff, C. F., Bernardello, R., Bopp, L., Brasika, I. B. M., Chamberlain, M. A., Chandra, N., Chevallier, F., Chini, L. P., Collier, N. O., Colligan, T. H., Cronin, M., Djeutchouang, L. M., Dou, X., Enright, M. P., Enyo, K., Erb, M., Evans, W., Feely, R. A., Feng, L., Ford, D. J., Foster, A., Fransner, F., Gasser, T., Gehlen, M., Gkritzalis, T., Goncalves De Souza, J., Grassi, G., Gregor, L., Gruber, N., Guenet, B., Gürses, Ö., Harrington, K., Harris, I., Heinke, J., Hurtt, G. C., Iida, Y., Ilyina, T., Ito, A., Jacobson, A. R., Jain, A. K., Jarníková, T., Jersild, A., Jiang, F., Jones, S. D., Kato, E., Keeling, R. F., Klein Goldewijk, K., Knauer, J., Kong, Y., Korsbakken, J. I., Koven, C., Kunimitsu, T., Lan, X., Liu, J., Liu, Z., Liu, Z., Lo Monaco, C., Ma, L., Marland, G., McGuire, P. C., McKinley, G. A., Melton, J. R., Monacci, N., Monier, E., Morgan, E. J., Munro, D. R., Müller, J. D., Nakaoka, S.-I., Nayagam, L. R., Niwa, Y., Nutzel, T., Olsen, A., Omar, A. M., Pan, N., Pandey, S., Pierrot, D., Qin, Z., Regnier, P., Rehder, G., Resplandy, L., Roobaert, A., Rosan, T. M., Rödenbeck, C., Schwinger, J., Skjelvan, I., Smallman, T. L., Spada, V., Sreeush, M. G., Sun, Q., Sutton, A. J., Sweeney, C., Swingedouw, D., Séférian, R., Takao, S., Tatebe, H., Tian, H., Tian, X., Tilbrook, B., Tsujino, H., Tubiello, F., van Ooijen, E., van der Werf, G. R., van de Velde, S. J.,

https://doi.org/10.5194/egusphere-2026-3864
Preprint. Discussion started: 17 July 2026

Walker, A. P., Wanninkhof, R., Yang, X., Yuan, W., Yue, X., and Zeng, J.: Global Carbon Budget 2025, Earth System Science Data, 18, 3211-3288, https://doi.org/10.5194/essd-18-3211-2026, 2026.

Han, G., Ma, X., Liang, A., Zhang, T., Zhao, Y., Zhang, M., and Gong, W.: Performance Evaluation for China's Planned CO2-IPDA, 10.3390/rs9080768, 2017.

Han, G., Xu, H., Gong, W., Liu, J., Du, J., Ma, X., and Liang, A.: Feasibility Study on Measuring Atmospheric CO2 in Urban Areas Using Spaceborne CO2-IPDA LIDAR, 10.3390/rs10070985, 2018.

Han, G., Huang, Y., Shi, T., Zhang, H., Li, S., Zhang, H., Chen, W., Liu, J., and Gong, W.: Quantifying CO2 emissions of power plants with Aerosols and Carbon Dioxide Lidar onboard DQ-1, Remote Sensing of Environment, 313, 114368, https://doi.org/10.1016/j.rse.2024.114368, 2024.

Han, G., Zhang, H., Huang, Y., Chen, W., Mao, H., Zhang, X., Ma, X., Li, S., Zhang, H., Liu, J., Mao, F., and Gong, W.: First global XCO2 observations from spaceborne lidar: methodology and initial result, Remote Sensing of Environment, 330, 114954, https://doi.org/10.1016/j.rse.2025.114954, 2025.

Ji, M., Xu, Y., Zhang, Y., Mo, Y., Zhu, S., Wang, W., Zhou, M., Morino, I., Ohyama, H., Shiomi, K., and Oh, Y.-S.: Validation of Remotely Sensed XCO2 Products With TCCON Observations in East Asia, IEEE Journal of Selected Topics in Applied Earth Observations and Remote Sensing, 17, 7159-7169, https://doi.org/10.1109/jstars.2024.3378229, 2024.

Keppel-Aleks, G., Wennberg, P. O., O'Dell, C. W., and Wunch, D.: Towards constraints on fossil fuel emissions from total column carbon dioxide, Atmospheric Chemistry and Physics, 13, 4349-4357, https://doi.org/10.5194/acp-13-4349-2013, 2013.

Kong, Y., Chen, B., and Measho, S.: Spatio-Temporal Consistency Evaluation of XCO2 Retrievals from GOSAT and OCO-2 Based on TCCON and Model Data for Joint Utilization in Carbon Cycle Research, Atmosphere, 10, 354, https://doi.org/10.3390/atmos10070354, 2019.

Kulawik, S., Wunch, D., O'Dell, C., Frankenberg, C., Reuter, M., Oda, T., Chevallier, F., Sherlock, V., Buchwitz, M., Osterman, G., Miller, C. E., Wennberg, P. O., Griffith, D., Morino, I., Dubey, M. K., Deutscher, N. M., Notholt, J., Hase, F., Warneke, T., Sussmann, R., Robinson, J., Strong, K., Schneider, M., De Mazière, M., Shiomi, K., Feist, D. G., Iraci, L. T., and Wolf, J.: Consistent evaluation of ACOS-GOSAT, BESD-SCIAMACHY, CarbonTracker, and MACC through comparisons to TCCON, Atmospheric Measurement Techniques, 9, 683-709, https://doi.org/10.5194/amt-9-683-2016, 2016.

Kuze, A., Suto, H., Nakajima, M., and Hamazaki, T.: Thermal and near infrared sensor for carbon observation Fourier-transform spectrometer on the Greenhouse Gases Observing Satellite for greenhouse gases monitoring, Applied Optics, 48, 6716, https://doi.org/10.1364/ao.48.006716, 2009.

Kuze, A., Suto, H., Shiomi, K., Kawakami, S., Tanaka, M., Ueda, Y., Deguchi, A., Yoshida, J., Yamamoto, Y., Kataoka, F., Taylor, T. E., and Buijs, H. L.: Update on GOSAT TANSO-FTS performance, operations, and data products after more than 6 years in space, Atmospheric Measurement Techniques, 9, 2445-2461, https://doi.org/10.5194/amt-9-2445-2016, 2016.

Liang, A., Gong, W., Han, G., and Xiang, C.: Comparison of Satellite-Observed XCO2 from GOSAT, OCO-2, and Ground-Based TCCON, Remote Sensing, 9, 1033, https://doi.org/10.3390/rs9101033, 2017.

Mao, J., Ramanathan, A., Abshire, J. B., Kawa, S. R., Riris, H., Allan, G. R., Rodriguez, M., Hasselbrack, W. E., Sun, X., Numata, K., Chen, J., Choi, Y., and Yang, M. Y. M.: Measurement of atmospheric CO2 column concentrations to cloud tops with a pulsed multi-wavelength airborne lidar, Atmospheric Measurement Techniques, 11, 127-140, https://doi.org/10.5194/amt-11-127-2018, 2018.

Noël, S., Reuter, M., Buchwitz, M., Borchardt, J., Hilker, M., Bovensmann, H., Burrows, J. P., Di Noia, A., Suto, H., Yoshida, Y., Buschmann, M., Deutscher, N. M., Feist, D. G., Griffith, D. W. T., Hase, F., Kivi, R., Morino, I., Notholt, J., Ohyama, H., Petri, C., Podolske, J. R., Pollard, D. F., Sha, M. K., Shiomi, K., Sussmann, R., Té, Y., Velazco, V. A., and Warneke, T.: XCO2 retrieval for GOSAT and GOSAT-2 based on the FOCAL algorithm, Atmospheric Measurement Techniques, 14, 3837-3869, https://doi.org/10.5194/amt-14-3837-2021, 2021.

Noël, S., Reuter, M., Buchwitz, M., Borchardt, J., Hilker, M., Schneising, O., Bovensmann, H., Burrows, J. P., Di Noia, A., Parker, R. J., Suto, H., Yoshida, Y., Buschmann, M., Deutscher, N. M., Feist, D. G., Griffith, D. W. T., Hase, F., Kivi, R., Liu, C., Morino, I., Notholt, J., Oh, Y.-S., Ohyama, H., Petri, C., Pollard, D. F., Rettinger, M., Roehl, C., Rousogenous, C., Sha, M. K., Shiomi, K., Strong, K., Sussmann, R., Té, Y., Velazco, V. A., Vrekoussis, M., and Warneke, T.: Retrieval of greenhouse gases from GOSAT and GOSAT-2 using the FOCAL algorithm, Atmospheric Measurement Techniques, 15, 3401-3437, https://doi.org/10.5194/amt-15-3401-2022, 2022.

O'Dell, C. W., Eldering, A., Wennberg, P. O., Crisp, D., Gunson, M. R., Fisher, B., Frankenberg, C., Kiel, M., Lindqvist, H., Mandrake, L., Merrelli, A., Natraj, V., Nelson, R. R., Osterman, G. B., Payne, V. H., Taylor, T. E., Wunch, D., Drouin, B. J., Oyafuso, F., Chang, A., McDuffie, J., Smyth, M., Baker, D. F., Basu, S., Chevallier, F., Crowell, S. M. R., Feng, L., Palmer, P. I., Dubey, M., García, O. E., Griffith, D. W. T., Hase, F., Iraci, L. T., Kivi, R., Morino, I., Notholt, J., Ohyama, H., Petri, C., Roehl, C. M., Sha, M. K., Strong, K., Sussmann, R., Te, Y., Uchino, O., and Velazco, V. A.: Improved retrievals of carbon dioxide from Orbiting Carbon Observatory-2 with the version 8 ACOS algorithm, Atmospheric Measurement Techniques, 11, 6539-6576, https://doi.org/10.5194/amt-11-6539-2018, 2018.

Shi, T., Han, G., Ma, X., Pei, Z., Chen, W., Liu, J., Zhang, X., Li, S., and Gong, W.: Quantifying strong point sources emissions of CO2 using spaceborne LiDAR: Method development and potential analysis, Energy Conversion and Management, 292, 117346, https://doi.org/10.1016/j.enconman.2023.117346, 2023.

Suto, H., Kataoka, F., Kikuchi, N., Knuteson, R. O., Butz, A., Haun, M., Buijs, H., Shiomi, K., Imai, H., and Kuze, A.: Thermal and near-infrared sensor for carbon observation Fourier transform spectrometer-2 (TANSO-FTS-2) on the Greenhouse gases Observing SATellite-2 (GOSAT-2) during its first year in orbit, Atmospheric Measurement Techniques, 14, 2013-2039, https://doi.org/10.5194/amt-14-2013-2021, 2021.

Taylor, T. E., O'Dell, C. W., Baker, D., Bruegge, C., Chang, A., Chapsky, L., Chatterjee, A., Cheng, C., Chevallier, F., Crisp, D., Dang, L., Drouin, B., Eldering, A., Feng, L., Fisher, B., Fu, D., Gunson, M., Haemmerle, V., Keller, G. R., Kiel, M., Kuai, L., Kurosu, T., Lambert, A., Laughner, J., Lee, R., Liu, J., Mandrake, L., Marchetti, Y., McGarragh, G., Merrelli,

https://doi.org/10.5194/egusphere-2026-3864
Preprint. Discussion started: 17 July 2026

A., Nelson, R. R., Osterman, G., Oyafuso, F., Palmer, P. I., Payne, V. H., Rosenberg, R., Somkuti, P., Spiers, G., To, C., Weir, B., Wennberg, P. O., Yu, S., and Zong, J.: Evaluating the consistency between OCO-2 and OCO-3 XCO2 estimates derived from the NASA ACOS version 10 retrieval algorithm, Atmospheric Measurement Techniques, 16, 3173-3209, https://doi.org/10.5194/amt-16-3173-2023, 2023.

Vermote, E. F. and Kotchenova, S.: Atmospheric correction for the monitoring of land surfaces, Journal of Geophysical Research: Atmospheres, 113, 2007JD009662, https://doi.org/10.1029/2007jd009662, 2008.

Vermote, E. F., El Saleous, N. Z., and Justice, C. O.: Atmospheric correction of MODIS data in the visible to middle infrared: first results, Remote Sensing of Environment, 83, 97-111, https://doi.org/10.1016/s0034-4257(02)00089-5, 2002.

Vermote, E. F., El Saleous, N., Justice, C. O., Kaufman, Y. J., Privette, J. L., Remer, L., Roger, J. C., and Tanré, D.: Atmospheric correction of visible to middle-infrared EOS-MODIS data over land surfaces: Background, operational algorithm and validation, Journal of Geophysical Research: Atmospheres, 102, 17131-17141, https://doi.org/10.1029/97jd00201, 1997.

Wang, J. S., Kawa, S. R., Eluszkiewicz, J., Baker, D. F., Mountain, M., Henderson, J., Nehrkorn, T., and Zaccheo, T. S.: A regional CO2 observing system simulation experiment for the ASCENDS satellite mission, Atmospheric Chemistry and Physics, 14, 12897-12914, https://doi.org/10.5194/acp-14-12897-2014, 2014.

Wunch, D., Toon, G. C., Blavier, J.-F. L., Washenfelder, R. A., Notholt, J., Connor, B. J., Griffith, D. W. T., Sherlock, V., and Wennberg, P. O.: The Total Carbon Column Observing Network, Philosophical Transactions of the Royal Society A: Mathematical, Physical and Engineering Sciences, 369, 2087-2112, https://doi.org/10.1098/rsta.2010.0240, 2011.

Wunch, D., Toon, G. C., Wennberg, P. O., Wofsy, S. C., Stephens, B. B., Fischer, M. L., Uchino, O., Abshire, J. B., Bernath, P., Biraud, S. C., Blavier, J. F. L., Boone, C., Bowman, K. P., Browell, E. V., Campos, T., Connor, B. J., Daube, B. C., Deutscher, N. M., Diao, M., Elkins, J. W., Gerbig, C., Gottlieb, E., Griffith, D. W. T., Hurst, D. F., Jiménez, R., Keppel-Aleks, G., Kort, E. A., Macatangay, R., Machida, T., Matsueda, H., Moore, F., Morino, I., Park, S., Robinson, J., Roehl, C. M., Sawa, Y., Sherlock, V., Sweeney, C., Tanaka, T., and Zondlo, M. A.: Calibration of the Total Carbon Column Observing Network using aircraft profile data, Atmospheric Measurement Techniques, 3, 1351-1362, https://doi.org/10.5194/amt-3-1351-2010, 2010.

Wunch, D., Wennberg, P. O., Osterman, G., Fisher, B., Naylor, B., Roehl, C. M., O'Dell, C., Mandrake, L., Viatte, C., Kiel, M., Griffith, D. W. T., Deutscher, N. M., Velazco, V. A., Notholt, J., Warneke, T., Petri, C., De Maziere, M., Sha, M. K., Sussmann, R., Rettinger, M., Pollard, D., Robinson, J., Morino, I., Uchino, O., Hase, F., Blumenstock, T., Feist, D. G., Arnold, S. G., Strong, K., Mendonca, J., Kivi, R., Heikkinen, P., Iraci, L., Podolske, J., Hillyard, P. W., Kawakami, S., Dubey, M. K., Parker, H. A., Sepulveda, E., García, O. E., Te, Y., Jeseck, P., Gunson, M. R., Crisp, D., and Eldering, A.: Comparisons of the Orbiting Carbon Observatory-2 (OCO-2) XCO2 measurements with TCCON, Atmospheric Measurement Techniques, 10, 2209-2238, https://doi.org/10.5194/amt-10-2209-2017, 2017.

Yang, D., Boesch, H., Liu, Y., Somkuti, P., Cai, Z., Chen, X., Di Noia, A., Lin, C., Lu, N., Lyu, D., Parker, R. J., Tian, L., Wang, M., Webb, A., Yao, L., Yin, Z., Zheng, Y., Deutscher, N. M., Griffith, D. W. T., Hase, F., Kivi, R., Morino, I.,

https://doi.org/10.5194/egusphere-2026-3864
Preprint. Discussion started: 17 July 2026

Notholt, J., Ohyama, H., Pollard, D. F., Shiomi, K., Sussmann, R., Té, Y., Velazco, V. A., Warneke, T., and Wunch, D.: Toward High Precision XCO2 Retrievals From TanSat Observations: Retrieval Improvement and Validation Against TCCON Measurements, Journal of Geophysical Research: Atmospheres, 125, e2020JD032794, https://doi.org/10.1029/2020jd032794, 2020.

Yang, H., Li, T., Wu, J., and Zhang, L.: Inter-comparison and evaluation of global satellite XCO2 products, Geo-spatial Information Science, 28, 131-144, https://doi.org/10.1080/10095020.2023.2252017, 2025.

Yi, J., Huang, Y., Pei, Z., and Han, G.: Urban Area Observing System (UAOS) simulation experiment using DQ-1 total column concentration observations, Atmospheric Chemistry and Physics, 25, 13687-13710, https://doi.org/10.5194/acp-25-13687-2025, 2025.

Yi, J., Huang, Y., Han, G., Zhang, H., Pei, Z., Luo, H., Zhang, Y., Shi, T., Li, S., and Gong, W.: Active and passive satellite observations coupled with carbon–nitrogen synergy for urban fossil fuel CO2 emissions monitoring, Atmospheric Chemistry and Physics, 26, 8475-8504, https://doi.org/10.5194/acp-26-8475-2026, 2026.

Yoshida, Y., Someya, Y., Ohyama, H., Morino, I., Matsunaga, T., Deutscher, N. M., Griffith, D. W. T., Hase, F., Iraci, L. T., Kivi, R., Notholt, J., Pollard, D. F., Té, Y., Velazco, V. A., and Wunch, D.: Quality Evaluation of the Column-Averaged Dry Air Mole Fractions of Carbon Dioxide and Methane Observed by GOSAT and GOSAT-2, SOLA, 19, 173-184, https://doi.org/10.2151/sola.2023-023, 2023.

Yoshida, Y., Kikuchi, N., Morino, I., Uchino, O., Oshchepkov, S., Bril, A., Saeki, T., Schutgens, N., Toon, G. C., Wunch, D., Roehl, C. M., Wennberg, P. O., Griffith, D. W. T., Deutscher, N. M., Warneke, T., Notholt, J., Robinson, J., Sherlock, V., Connor, B., Rettinger, M., Sussmann, R., Ahonen, P., Heikkinen, P., Kyrö, E., Mendonca, J., Strong, K., Hase, F., Dohe, S., and Yokota, T.: Improvement of the retrieval algorithm for GOSAT SWIR XCO2 and XCH4 and their validation using TCCON data, Atmospheric Measurement Techniques, 6, 1533-1547, https://doi.org/10.5194/amt-6-1533-2013, 2013.

Zhang, H., Han, G., Chen, W., Pei, Z., Liu, B., Liu, J., Zhang, T., Li, S., and Gong, W.: Validation Method for Spaceborne IPDA LIDAR XCO2 Products via TCCON, IEEE Journal of Selected Topics in Applied Earth Observations and Remote Sensing, 17, 16984-16992, https://doi.org/10.1109/jstars.2024.3418028, 2024.

Zhang, X., Yang, H., Bu, L., Fan, Z., Xiao, W., Chen, B., Zhang, L., Liu, S., Wang, Z., Liu, J., Chen, W., and Lee, X.: Estimation of diurnal emissions of CO2 from thermal power plants using spaceborne integrated path differential absorption (IPDA) lidar, Atmospheric Chemistry and Physics, 25, 6725-6740, https://doi.org/10.5194/acp-25-6725-2025, 2025.